# NEURAL SUPER-RESOLUTION FOR MESH-BASED SIM-ULATIONS UNDER SCARCE SUPERVISION

**Anonymous authors**Paper under double-blind review

000

001

002003004

006

008 009

010 011

012

013

014

016

017

018

019

021

023

025

026

027

028

031 032 033

037

040

041

042

043

044

046

047

048

051

052

#### **ABSTRACT**

Mesh-based simulations provide high-fidelity solutions to partial differential equations (PDEs), but achieving such accuracy typically requires fine meshes, leading to substantial computational overhead. Super-resolution techniques aim to mitigate this cost by reconstructing high-resolution (HR), high-fidelity solutions from low-cost, low-resolution (LR) counterparts. However, training neural networks for super-resolution often demands large amounts of expensive HR supervision data, posing a major practical limitation. To address this challenge, we propose SuperMeshNet, an HR data-efficient super-resolution framework for mesh-based simulations aided by message passing neural networks (MPNNs). As its core, SuperMeshNet introduces complementary learning that effectively leverages both a small amount of paired LR-HR data and abundant unpaired LR data via two jointly trained, complementary MPNN-based models. Theses models are enriched by task-specific **inductive biases** that emphasize local variations critical for accurate super-resolution. Extensive experiments demonstrate that SuperMeshNet—an MPNN-based model with inductive biases trained on a dataset with 10% paired LR-HR data and 90% unpaired LR data—achieves an even lower root mean square error (RMSE) than the same MPNN without inductive biases trained on 100% of LR-HR pairs, while in turn requiring 90% less HR data. The source code and datasets are available at https://anonymous.4open.science/r/SuperMeshNet/README.md.

## 1 Introduction

Mesh-based simulations—such as the finite element method (FEM), finite volume method (FVM), or computational fluid dynamics (CFD)—are widely used to obtain high-fidelity solutions to partial differential equations (PDEs) across a range of scientific and engineering domains. In mesh-based simulations, the mesh size is carefully chosen to balance computational costs against solution fidelity: finer meshes offer higher fidelity but incur significantly greater computational expenses (Obiols-Sales et al., 2024). Super-resolution techniques are developed to alleviate this trade-off by predicting high-resolution (HR) simulation results from low-resolution (LR) counterparts, thereby aiming to deliver high-fidelity solutions at a reduced cost (Barwey et al., 2024; Obiols-Sales et al., 2024). However, training super-resolution models via conventional fully supervised learning demands substantial quantities of computationally expensive HR training data, making data collection a significant bottleneck (Obiols-Sales et al., 2024). In this context, improving the HR data efficiency of super-resolution model training is of paramount importance in reality.

As summarized in Table 1, several unsupervised learning approaches tackled this challenge but pose their own limitations. For example, PhysRNet (Arora, 2022) performs super-resolution without any HR training data by incorporating PDEs and constraints into its loss function; however, PhysRNet uses a finite-difference scheme for derivative calculations, which limits its applicability to irregular meshes. MAgNet (Boussif et al., 2022) offers an alternative with zero-shot super-resolution through an interpolator trained on LR data; yet, the prediction error of MAgNet is much larger than that of supervised methods (see Appendix I). To the best of our knowledge, *semi-supervised learning* has not been applied to the super-resolution task for mesh-based simulations. This may be partly due to the limited exploration of semi-supervised regression methods, especially those compatible with message passing neural networks (MPNNs), compared to semi-supervised classification. Refer to Appendix C for detailed explanations and limitations of existing semi-supervised regression approaches.

Table 1: Comparison between prior studies and our work. Here,  $r = \frac{\text{number of HR data samples}}{\text{number of LR data samples}}$ 

Reference	Learning method	Model
Li and McComb (2022), Yonekura et al. (2023), Obiols-Sales et al. (2024)	fully supervised $(r=1)$	CNN
de Avila Belbute-Peres et al. (2020), Barwey et al. (2024)	fully supervised $(r=1)$	MPNN
Arora (2022)	unsupervised $(r=0)$	CNN
Boussif et al. (2022)	unsupervised $(r=0)$	MPNN
SuperMeshNet (ours)		MPNN (inductive biases)

Many related studies (Yonekura et al., 2023; Arora, 2022; Li and McComb, 2022; Obiols-Sales et al., 2024) on super-resolution for mesh-based simulations rely heavily on convolutional neural networks (CNNs), which cannot directly handle irregular mesh structures. CNNs require interpolating irregular mesh-based data onto a regular grid, which often necessitates a significantly larger number of nodes to achieve the same fidelity as an irregular mesh, leading to relatively lower computational efficiency. Some studies have adopted MPNNs, such as graph convolutional networks (GCNs) (de Avila Belbute-Peres et al., 2020) or SRGNN (Barwey et al., 2024), which can directly handle irregular mesh data. However, the task-specific design of inductive biases for improving mesh-based super-resolution performance remains largely underexplored.

To address these limitations, we propose SuperMeshNet, an HR data-efficient super-resolution framework tailored for mesh-based simulations under very scarce HR supervision, which basically differs from the supervised and unsupervised settings. To the best of our knowledge, this is the first general framework that can be applied across diverse MPNN architectures for the super-resolution task. To be specific, SuperMeshNet introduces two key components: complementary learning and **inductive biases for MPNNs.** First, the **complementary learning** is a novel *semi-supervised* learning method that exploits a small amount of paired LR-HR training data for supervised learning, while judiciously leveraging a large pool of unpaired LR data in an unsupervised manner. Our complementary learning is built upon two models; an MPNN-based primary model predicts HR solutions from LR counterparts, while an MPNN-based auxiliary model predicts the difference between two HR solutions corresponding to two LR counterparts. The predictions from each model are utilized to calculate pseudo-ground truths, which serve as ground truth for the other, enabling mutual supervision. Since conventional semi-supervised methods typically employ two identical models, they often produce highly similar pseudo-ground truths, making them less informative. On the other hand, owing to distinct but interrelated input-output configurations of our complementary learning, the auxiliary model captures intra-resolution relation while the primary model focuses on inter-resolution relation. This division of roles fosters synergies in mutual supervision, enhancing super-resolution performance while reducing training time compared to prior semi-supervised strategies.

Second, to improve the performance of mesh-based super-resolution, we introduce **inductive biases for MPNNs**, guided by the empirical observation that local deviations carry richer super-resolution information than the global mean. Specifically, we propose two MPNN-architecture-agnostic inductive biases: **node-level centering** and **message-level centering**. The node-level centering centers each node embedding by subtracting the global mean of all node embeddings from each node embedding, while the message-level centering performs a similar centering operation over aggregated messages. Subtracting the global mean removes redundant background information and highlights fine-grained variations that are critical for super-resolution.

We carry out extensive experiments to validate the effectiveness of our two components in SuperMeshNet. Our results demonstrate that, even with only a small portion (*e.g.*, 10%) of paired LR–HR data, SuperMeshNet surpasses a fully supervised (*e.g.*, 100% paired) benchmark method lacking inductive biases in terms of the root mean square error (RMSE). We also prove that the injected inductive biases consistently reduce the RMSE across six different MPNN architectures, underscoring their general applicability. Finally, our main contributions are summarized as follows:

- MPNN-agnostic applicability. SuperMeshNet provides a general super-resolution framework for mesh-based simulations, applicable to various MPNNs, under very scarce HR supervision scenarios.
- Complementary learning. To the best of our knowledge, this is the first attempt to incorporate semisupervised learning compatible with MPNNs into super-resolution for the mesh-based simulations.
- **Inductive biases.** We introduce node-level centering and message-level centering, which can substantially enhance super-resolution performance across different MPNN types.

# 2 METHODOLOGY<sup>1</sup>

#### 2.1 PROBLEM DEFINITION

Briefly, we aim to predict an HR solution  $\hat{u}_h$  from an LR solution  $u_l$  of the same PDE, while relying on as few HR solutions  $u_h$  as possible for training. Formally, let  $\Omega \subset \mathbb{R}^D$  be the computational domain on which the PDE is solved. Here, D denotes the spatial dimension. A parameter  $\mu$  represents all variations of PDE instances, such as material coefficients, domain geometry, or boundary conditions. For example,  $\mu$  could be an angle of an applied force or an aspect ratio of an elliptical hole (see Figures 9–11 in Appendix H). Each choice of  $\mu$  defines a different

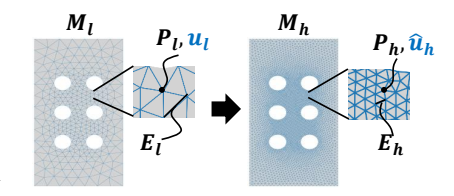


Figure 1: Problem setting. We aim to make prediction  $\hat{u}_h$  on HR mesh  $M_h$ , containing nodes at positions  $P_h$  and edges  $E_h$ , from LR data sample  $u_l$  defined on LR mesh  $M_l$ , comprising nodes at positions  $P_l$  and edges  $E_l$ .

PDE instance. We discretize  $\Omega$  with an LR mesh  $M_l = (P_l, E_l)$  and an HR mesh  $M_h = (P_h, E_h)$ , where  $P_l \in \mathbb{R}^{n_l \times D}$  and  $P_h \in \mathbb{R}^{n_h \times D}$  are the positions of the nodes on  $M_l$  and  $M_h$ , respectively, and  $E_l$  and  $E_h$  are edges on  $M_l$  and  $M_h$ , respectively. Running a PDE solver on these meshes yields: LR and HR solutions, which we regard as an LR data sample  $u_l$  and an HR data sample  $u_h$ , defined on the nodes on  $M_l$  and  $M_h$ , respectively. Our objective is to predict  $\hat{u}_h \in \mathbb{R}^{n_h \times d}$  from  $u_l$  as closely as possible to  $u_h$ , while minimizing the amount of HR data  $u_h$  required for training, where d denotes the dimension of the solution field.

#### 2.2 Complementary Learning

#### 2.2.1 Dataset Setting

As depicted in Figure 2, the complementary learning leverages both a paired LR–HR training dataset  $\mathcal{D}_a = \{(u_l^q, u_h^q) \mid q=1, 2, \cdots, N_h\}$  having  $N_h$  LR–HR data samples and an unpaired LR training dataset  $\mathcal{D}_b = \{u_l^q \mid q=N_{h+1}, N_{h+2}, \cdots, N\}$  having  $N-N_h$  LR data samples. The total number of LR data samples is N, among which only  $N_h$  have HR counterparts, with  $N_h \ll N$  in practice. In other words,  $N-N_h$  fewer HR data samples are required compared to fully supervised learning. Here, the superscript q is simply an index to distinguish different samples corresponding to different parameters  $\mu$ . For instance, if  $\mu$  is the angle of an applied force, then  $(u_l^1, u_h^1)$  corresponds to one angle  $\mu^1$ , and  $(u_l^2, u_h^2)$  corresponds to another  $\mu^2$ .



Figure 2: Dataset setting. Complementary learning utilizes a paired LR–HR training dataset, including  $N_h$  paired data samples (green hexagons), and an unpaired LR training dataset, containing  $N-N_h$  unpaired LR data samples (white hexagons). In total, complementary learning can reduce  $N-N_h$  HR data samples compared to the case of fully supervised learning.

## 2.2.2 The Two Models: $F_{\theta}$ and $G_{\phi}$

To fully exploit unpaired LR training data, the complementary learning utilizes mutual supervision between two models, namely,  $F_{\theta}$  and  $G_{\phi}$ , trained jointly under different roles. The primary model  $F_{\theta}$ , which is used for inference only, predicts an HR solution  $\hat{u}_h^q$  from its LR counterpart  $u_l^q$ :

$$F_{\theta}(u_{l}^{q}) = \hat{u}_{h}^{q} \quad (\text{ground truth} : u_{h}^{q}).$$
 (1)

On the other hand, the auxiliary model  $G_{\phi}$ , which is used only during training, predicts the **difference between two HR** solutions  $\hat{u}_h^{rs}$  corresponding to two LR input samples  $u_l^r, u_l^s$  to further utilize intra-resolution relations. Here, r and s indicate two LR samples corresponding to different  $\mu$ 's. Since computational geometry may vary across samples with different  $\mu$ ,  $u_h^r$  and  $u_h^s$  may be defined on different positions  $P_h^r$  and  $P_h^s$ . Thus, direct subtraction is not possible. To resolve this, we apply k-nearest neighbor (k NN) interpolation (Qi et al., 2017) to project solutions defined on  $P_h^s$  onto  $P_h^r$ :

$$G_{\phi}(u_l^r, u_l^s) = \hat{u}_h^{rs} \quad (\text{ground truth} : u_h^r - kNN(u_h^s; P_h^s \to P_h^r)). \tag{2}$$

Detailed calculation of kNN interpolation and architectures of  $F_{\theta}$  and  $G_{\phi}$  are available in Appendices E and F, respectively.

<sup>&</sup>lt;sup>1</sup>Notations are summarized in Appendix B.

#### 2.2.3 Learning Procedure via Our Loss

As depicted in Figure 3, each training step combines supervised and unsupervised learning of both  $F_{\theta}$  and  $G_{\phi}$ . In other words, the loss functions for training  $F_{\theta}$  and  $G_{\phi}$ , denoted by  $\mathcal{L}_F$  and  $\mathcal{L}_G$ , respectively, are expressed as:

$$\mathcal{L}_F = \mathcal{L}_{F,sup} + \mathcal{L}_{F,unsup} \tag{3}$$

$$\mathcal{L}_G = \mathcal{L}_{G,sup} + \mathcal{L}_{G,unsup},\tag{4}$$

where the subscripts sup and unsup represent supervised and unsupervised learning, respectively. To this end, three samples are randomly sampled: 1) two paired LR samples  $u_l^{\alpha}$  and  $u_l^{\beta}$  from the paired LR–HR dataset  $\mathcal{D}_a$  for supervised learning and 2) one additional unpaired LR sample  $u_l^{\gamma}$  from the unpaired LR dataset  $\mathcal{D}_b$  for unsupervised learning. Here,  $\alpha$ ,  $\beta$ , and  $\gamma$  are the indices referring to distinct parameters  $\mu$ .

In supervised learning, an HR data sample  $u_h^{\alpha}$  is available. As depicted in Figure 3,  $F_{\theta}$  is trained to reduce the MSE between its prediction  $\hat{u}_h^{\alpha}$  and its target, which is the ground truth  $u_h^{\alpha}$ . An analogous procedure is applied to  $\beta$ , thus resulting in:

$$L_{F,sup} = \ell(\hat{u}_h^{\alpha}, u_h^{\alpha}) + \ell(\hat{u}_h^{\beta}, u_h^{\beta}), \tag{5}$$

where  $\ell(\cdot,\cdot)$  denotes the MSE. Similarly, as expressed in Eq. (2),  $G_{\phi}$  is trained to reduce the MSE between its predictions  $\hat{u}_h^{\alpha\beta}$  and its target, which is the ground truth difference between  $u_h^{\alpha}$  and  $u_h^{\beta}$  alongside the following loss:

$$\mathcal{L}_{G,sup} = \ell(\hat{u}_h^{\alpha\beta}, u_h^{\alpha} - kNN(u_h^{\beta}; P_h^{\beta} \to P_h^{\alpha})). \tag{6}$$

In unsupervised learning, the ground truth HR data sample  $u_h^{\gamma}$  is unavailable. Under this circumstance, we leverage  $\mathit{mutual supervision}$  between  $F_{\theta}$  and  $G_{\phi}$ . For example, as depicted in Figure 3, if  $G_{\phi}(u_l^{\gamma}, u_l^{\alpha})$  predicts  $\hat{u}_h^{\gamma\alpha}$  that approximates the difference  $u_h^{\gamma} - u_h^{\alpha}$ , then adding this to the known  $u_h^{\alpha}$  yields an estimate of  $u_h^{\gamma}$ . This pseudo-ground truth can serve as a target for  $F_{\theta}(u_l^{\gamma})$ . Similarly, if  $F_{\theta}(u_l^{\gamma})$  produces  $\hat{u}_h^{\gamma}$  close to  $u_h^{\gamma}$ , then subtracting known  $u_h^{\alpha}$  from  $\hat{u}_h^{\gamma}$  provides an approximation of  $u_h^{\gamma} - u_h^{\alpha}$ , which can serve as a target for  $G_{\phi}(u_l^{\gamma}, u_l^{\alpha})$ , accordingly. An analogous procedure is applied to the pair  $(\beta, \gamma)$ . It should be noted that a thorough treatment of kNN interpolation is also required to effectively handle mesh mismatches. For example, in Eq. (7),  $u_h^{\beta} - \hat{u}_h^{\beta\gamma}$  can be used to approximate  $u_h^{\gamma}$ . However, the values are defined on  $P_h^{\beta}$ , whereas  $\hat{u}_h^{\gamma}$  is defined on  $P_h^{\gamma}$ . To reconcile this discrepancy, kNN interpolation is employed to project the values from  $P_h^{\gamma}$  onto  $P_h^{\beta}$ . The resultant loss functions are:

$$\mathcal{L}_{F,unsup} = \ell(\hat{u}_h^{\gamma}, \hat{u}_h^{\gamma\alpha} + kNN(u_h^{\alpha}; P_h^{\alpha} \to P_h^{\gamma})) + \ell(\hat{u}_h^{\gamma}, kNN(u_h^{\beta} - \hat{u}_h^{\beta\gamma}; P_h^{\beta} \to P_h^{\gamma})) \tag{7}$$

$$\mathcal{L}_{G,unsup} = \ell(\hat{u}_h^{\gamma\alpha}, \hat{u}_h^{\gamma} - kNN(u_h^{\alpha}; P_h^{\alpha} \to P_h^{\gamma})) + \ell(\hat{u}_h^{\beta\gamma}, u_h^{\beta} - kNN(\hat{u}_h^{\gamma}; P_h^{\gamma} \to P_h^{\beta})). \tag{8}$$

A pseudo-code for the complementary learning mechanism can be found in Appendix D.

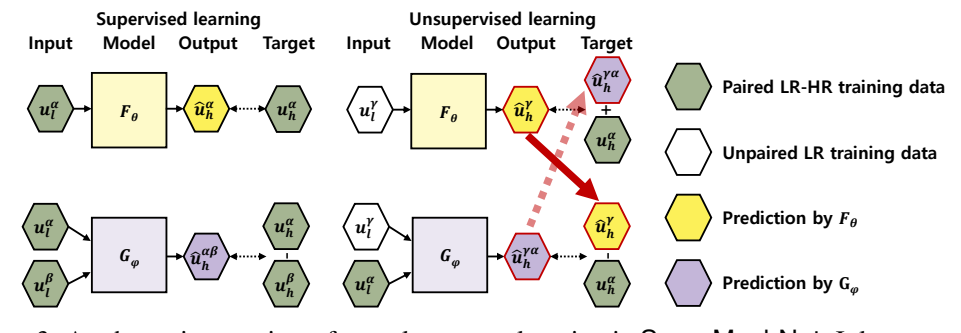


Figure 3: A schematic overview of complementary learning in SuperMeshNet. It leverages both supervised and unsupervised learning to jointly train two neural network models,  $F_{\theta}$  and  $G_{\phi}$ .  $F_{\theta}$  predicts an HR solution from its LR counterpart, while  $G_{\phi}$  predicts the difference between two HR solutions from two LR counterparts to enable synergistic mutual supervision. More specifically, for supervised learning,  $F_{\theta}$  and  $G_{\phi}$  are trained with pairs of LR–HR data (green hexagons). In unsupervised learning, the prediction of one model (yellow and purple hexagons predicted by  $F_{\theta}$  and  $G_{\phi}$ , respectively) is used to calculate a pseudo-ground truth that serves as the target for training another model (as depicted by sol;id and dotted red arrows).

#### 2.3 INDUCTIVE BIASES FOR MPNNS

Beyond our learning mechanism, we now turn to addressing our task-specific model. The two models,  $F_{\theta}$  and  $G_{\phi}$ , utilize MPNN layers (See Appendix F) to handle irregular mesh-based data. To further improve super-resolution performance, we incorporate two inductive biases into the message passing mechanism of each MPNN layer. This subsection first reviews conventional MPNNs, and then presents the two proposed inductive biases: node-level centering and message-level centering.

#### 2.3.1 PRELIMINARIES: MPNNS

MPNNs are a class of graph neural networks (GNNs) that propagate information across nodes using message passing mechanisms (Gilmer et al., 2020). In each MPNN layer, a target node i receives information, referred to as a message  $msg_{ij}$ , from its neighboring node  $j \in \mathcal{N}(i)$ . Here,  $msg_{ij}$  is typically a function of the source node's embedding  $x_j$ . Furthermore,  $msg_{ij}$  can be dependent on other factors such as the target node's embedding  $x_i$  or the edge embedding  $e_{ij}$ :

$$msg_{ij} = f_m(\lbrace x_j \rbrace \cup S_{ij}) \quad \text{for} \quad S_{ij} \subseteq \lbrace x_i, e_{ij} \rbrace,$$
 (9)

where  $f_m$  is a message function determined by the specific design of the MPNNs. Each node i aggregates messages  $msg_{ij}$  from its neighboring nodes j:

$$agg_i = \sum_{j \in \mathcal{N}(i)} msg_{ij}. \tag{10}$$

Finally, the node embedding  $x_i$  is updated based on its current embedding  $x_i$  and the aggregated message  $agg_i$ :

$$x_i \leftarrow f_x(x_i, agg_i), \tag{11}$$

where  $f_x$  is an update function determined by the types of MPNNs. The message aggregation in Eq. (10) and the node embedding update in Eq. (11) are repeated in the next MPNN layer. In some MPNNs, the message aggregation and the node embedding update steps are fused into a single step.

#### 2.3.2 Node-level centering

The first inductive bias, node-level centering, subtracts the mean of node embeddings  $x_i$ 's from each individual  $x_i$ :

$$x_i \leftarrow x_i - \frac{1}{n} \sum_{i=1}^n x_i,\tag{12}$$

where n denotes the number of nodes in LR mesh  $M_l$  or the number of nodes in HR mesh  $M_h$ . This step can be applied after the node embedding update step in Eq. (11). Refer to Appendix G for implementation details for each MPNN type. This inductive bias is motivated by the intuition that, in the super-resolution task, global mean information is less relevant, while *deviations* from the mean carry more meaningful signals. Experimental results (see Appendix J) show that subtracting the mean from LR data samples has minimal impact on super-resolution performance. This implies that the global mean is mostly uninformative in this context. By enforcing the node-level centering, MPNNs are encouraged to focus on deviations from the mean, leading to improved super-resolution performance.

#### 2.3.3 Message-level centering

For MPNNs employing an explicit two-step message passing mechanism, we experimentally found that removing mean component from the aggregated message  $agg_i$  also leads to super-resolution performance improvement. Specifically, the message-level centering subtracts the mean of the aggregated messages  $agg_i$ 's from the individual aggregated message  $agg_i$ :

$$agg_i \leftarrow agg_i - \frac{1}{n} \sum_{i=1}^n agg_i, \tag{13}$$

This message-level centering step can be applied between the message aggregation in Eq. (10) and the node embedding update in Eq. (11). Refer to Appendix G for implementation details for each MPNN type. Similarly as in the node-level centering, this helps MPNNs focus on deviations from the mean, which carry more informative signals in the context of super-resolution.

#### 3 EXPERIMENTAL RESULTS AND ANALYSES

272273274

Due to space limitations, we provide only a brief description of the experimental setup and a subset of experimental results in the main text. A detailed description of the datasets and the complete set of experiments is provided in Appendices H–S.

275276277

#### 3.1 Datasets

279280281282

278

**FEM Datasets.** FEM datasets used in our experiments are generated by solving PDEs utilizing FEniCSx, an open-source computing platform for FEM. Table 3 summarizes three datasets, detailing their governing PDEs, the quantities derived from solving these equations, the parameters that vary across the samples, and the number of nodes in LR and HR meshes. Dirichlet boundary conditions are utilized for all datasets.

283

Table 2: Summary of FEM datasets.

285286287

Dataset Equation Solution Parameter LR nodes HR nodes 1 Linear elasticity 333 4,053 von Mises stress Force angle 2 Linear elasticity von Mises stress Hole shape 329-387 3,959-4,157 3 324-388 Poisson equation Electric field Hole shape 3,959–4,154

288 289

290

291

292

293

294

295

**CFD Datasets.** To validate the applicability of SuperMeshNet to time-dependent PDEs and complex real-world geometry, we adopt two additional datasets generated by OpenFOAM (OpenCFD, 2024). The time-dependent PDE dataset is obtained by solving the incompressible Navier—Stokes equations for flow around a cylinder, whereas the real-world geometry dataset is constructed by solving the Laplace equation for potential flow around a motorbike with a rider. For the time-dependent PDE dataset, LR data samples are generated by downsampling HR data onto LR meshes. For all other datasets, LR data samples are obtained by independently solving the governing PDEs on LR meshes. Detailed descriptions of each dataset are provided in Appendix H. We refer to Section 3.7 to see results on CFD datasets and their relevant discussions.

296 297 298

Table 3: Summary of CFD datasets.

299 300 301

Dataset	Equation	Solution	Parameter	LR nodes	HR nodes
Time-dependent PDE	Incompressible Navier-Stokes	Speed	Time	576	7,440
Real-world geometry	Laplace	Pressure	Angle of attack	10,897	46,004

303 304

306 307

302

# 3.2 EXPERIMENTAL SETUP

We evaluate our methodology using six representative MPNNs, including GCN (Kipf and Welling, 2017), GraphSAGE (SAGE) (Hamilton et al., 2017), GAT (Veličković et al., 2018), Graph Transformer (GTR) (Shi et al., 2021), GIN (Xu et al., 2019), and MeshGraphNet (MGN) (Pfaff et al., 2021). Each MPNN consists of three layers for processing in LR and additional three layers for processing in HR, and hidden dimension of each layer is 30. Throughout the experiments, we adopt Adam optimizer with learning rate of  $1\times10^{-3}$  and PyTorch's automatic mixed precision training to improve computational efficiency. All experiments are carried out on a machine with Intel (R) Core (TM) i9-10920X CPUs@3.50 GHz and an NVIDIA RTX A6000 GPU. The RMSE is used as a metric where lower values indicate better performance.

315316317

314

#### 3.3 COMPARISON WITH FULL SUPERVISION

Table 4 compares the RMSE of each MPNN integrated with our framework SuperMeshNet, and its variant without inductive biases, SuperMeshNet-O, against two fully supervised baselines—the same type of MPNNs but trained with full supervision without inductive biases. SuperMeshNet-O trained with 20 HR data samples (i.e.,  $N_h=20$ ) and 200 LR data samples (i.e., N=20) achieves a significantly lower RMSE compared to the MPNNs trained exclusively on 20 paired LR–HR samples (i.e.,  $N_h=N=20$ ). The improvement is attributed to complementary learning, which is inherently designed to effectively leverage the 180 unpaired LR samples that fully supervised learning cannot

utilize. Remarkably, despite being trained only with 20 HR data samples, SuperMeshNet-O achieves RMSE values that are on par with the second fully supervised baseline trained with the entire 200 HR data samples (i.e.,  $N_h = N = 200$ ). SuperMeshNet, enriched by inductive biases, surpasses the second baseline in most cases, highlighting the efficacy of the proposed inductive biases tailored for super-resolution in improving performance. This implies the potential to reduce up to 90% of the effort required to generate HR training data. Furthermore, our findings consistently demonstrate the improvement of SuperMeshNet in terms of HR data efficiency across all six MPNNs. This underscores its versatility and effectiveness in enhancing super-resolution performance, regardless of types of underlying MPNN architectures.

Table 4: The RMSE of SuperMeshNet (with inductive biases) and SuperMeshNet-O (without inductive biases) trained with  $N_h=20~\mathrm{HR}$  data samples and  $N=200~\mathrm{LR}$  data samples across six MPNNs and three datasets, in comparison with two fully supervised MPNNs including 1)  $N_h=N=20~\mathrm{and}$  2)  $N_h=N=200$ . The best performer is highlighted as **bold**.

	, 10			ı.				
Method $N_h$ , $N$		MPNN						
	111041104	1.11, 1.	GCN	SAGE	GAT	GTR	GIN	MGN
_	Fully supervised	20, 20	0.0874	0.0876	0.0826	0.0758	0.0819	0.0655
set	Fully supervised	200, 200	0.0575	0.0544	0.0512	0.0450	0.0381	0.0228
Dataset	SuperMeshNet-O	20, 200	0.0613	0.0589	0.0544	0.0451	0.0404	0.0269
Õ	SuperMeshNet	20, 200	0.0431	0.0450	0.0457	0.0385	0.0277	0.0226
7	Fully supervised	20, 20	0.0972	0.1025	0.0983	0.0983	0.0775	0.0730
set	Fully supervised	200, 200	0.0624	0.0633	0.0637	0.0572	0.0534	0.0461
Dataset	SuperMeshNet-O	20, 200	0.0636	0.0664	0.0680	0.0631	0.0569	0.0514
Õ	SuperMeshNet	20, 200	0.0574	0.0624	0.0634	0.0600	0.0537	0.0507
3	Fully supervised	20, 20	0.0587	0.0611	0.0616	0.0513	0.0569	0.0523
set	Fully supervised	200, 200	0.0370	0.0340	0.0374	0.0329	0.0317	0.0243
Dataset	SuperMeshNet-O	20, 200	0.0380	0.0366	0.0375	0.0363	0.0316	0.0281
Õ	SuperMeshNet	20, 200	0.0297	0.0297	0.0310	0.0294	0.0258	0.0245

## 3.4 COMPARISON WITH SUPER-RESOLUTION COMPETITORS

Although the primary objective of SuperMeshNet is to improve super-resolution performance across a wide range of MPNNs rather than to outperform a specific state-of-theart method, we compare a special case of SuperMeshNet using MGN with the most recent and relevant benchmarks, SRGNN (Barwey et al., 2024) and MAgNet (Boussif et al., 2022), to further validate its effectiveness. The results in Table 5 signify that SuperMeshNet, even when trained with only 20 HR data samples, outperforms SRGNN (Barwey et al., 2024) trained with 200 HR data samples, underscoring its superior training data efficiency. Furthermore, the results demonstrate that SuperMeshNet significantly outperforms the unsupervised baseline, MAgNet (Boussif et al., 2022), even under minimal HR supervision ( $N_h$ =5).

Table 5: The RMSE of MGN-based SuperMeshNet trained with varying numbers of HR data samples  $N_h$  and a fixed N=200 LR data samples for Dataset 1 in comparison with SRGNN with full supervision (N= $N_h$ =200), and MAgNet with no supervision (N=200,  $N_h$ =0).

Methods	$N_h$	RMSE
	5	0.0447
SuperMeshNet	10	0.0280
Superiviesifivet	20	0.0226
	40	0.0191
SRGNN	200	0.0247
MAgNet	0	0.0979

# 3.5 COMPARISON WITH BENCHMARK SEMI-SUPERVISED REGRESSION METHODS

Table 6 compares complementary learning in SuperMeshNet against benchmark semi-supervised regression methods on Dataset 1, using MGN as an MPNN architecture for each method. As presented in Table 6, SuperMeshNet achieves the lowest RMSE while also exhibiting the shortest training time among all benchmark semi-supervised regression methods. The performance improvements achieved by SuperMeshNet likely stem from its inherent characteristics of using two complementary models. Mean-Teacher (Tarvainen and Valpola, 2017) and UCVME (Dai et al., 2023) employ two models to predict the same target, *i.e.*, an HR data sample. Similarly, TNNR (Wetzel et al., 2022) uses one twin

Table 6: Comparison with benchmark semi-supervised regression methods in terms of the RMSE and training time (in second). Here, MGN is employed as an MPNN for each method. Training is conducted when  $N_h = 20$  and N = 200 for Dataset 1. The best performer is highlighted as **bold**.

Methods	RMSE	Training time (s)
mean-teacher (Tarvainen and Valpola, 2017)	0.0325	693.84
TNNR (Wetzel et al., 2022)	0.0624	477.48
UCVME (Dai et al., 2023)	0.0293	1122.62
SuperMeshNet-O	0.0269	503.2
SuperMeshNet	0.0226	421

neural network to predict the difference between two HR data. On the other hand, SuperMeshNet employs the *complementary learning* mechanism that leverages two distinct yet cooperative models: primary model  $F_{\theta}$ , which learns to predict an HR data sample, and auxiliary  $G_{\phi}$ , which learns to predict the difference between two HR data samples, as formulated in Eq. (2). While  $F_{\theta}$  operates on single LR input,  $G_{\phi}$  utilizes two LR data samples along with one HR data sample, enabling the two models to make predictions from distinct informational viewpoints. This architectural design promotes diversity into the learning process (See Table 17 in Appendix N) .

#### 3.6 ABLATION STUDIES ON INDUCTIVE BIASES

Table 7 presents ablation results on the two inductive biases in SuperMeshNet, demonstrating their effect on super-resolution performance in terms of the RMSE across six different MPNNs<sup>2</sup>. For all MPNNs, the incorporation of node-level centering (N) and message-level centering (M) into the MPNN architecture leads to substantial improvements in super-resolution performance (*i.e.*, a lower RMSE) compared to MPNNs without inductive biases (O). We claim that this improvement may be attributed to the reduced reliance on global mean information and an increased emphasis on local deviations from the mean.

We investigate whether the proposed inductive biases encourage the models to focus on local deviations rather than global mean information by analyzing the sensitivity of super-resolution performance to perturbations in the node embedding  $x_i$  (see Eq. (11)) and the aggregated message  $agg_i$  (see Eq. (10)). Specifically, we quantify the change in the RMSE when additive Gaussian noise with standard deviation of 0.01 is applied either to the global mean component or to the deviation component of  $x_i$ 's and  $agg_i$ 's, where the results are summarized in Table 8 when MGN is used as an MPNN. In SuperMeshNet-O (without inductive biases), denoted as O in Table 8, the RMSE is highly sensitive to noise added to the mean component while remaining relatively unaffected by perturbations in the deviation component, indicating a Table 7: Ablation studies on inductive biases. The RMSE of SuperMeshNet across six MPNNs under four inductive bias conditions (O: without inductive biases, N: node-level centering, M: message-level centering, and N+M: both node-level and message-level centerings) trained with  $N_h=20$  and N=200 for Dataset 1 is compared. For each MPNN, the lowest RMSE value among the four inductive bias conditions is highlighted as **bold**.

MPNN	RMSE					
	О	N	M	N + M		
GCN	0.0613	0.0431	-	=		
SAGE	0.0589	0.0493	0.0528	0.0450		
GAT	0.0544	0.0457	-	-		
GTR	0.0451	0.0405	0.0438	0.0385		
GIN	0.0404	0.0290	0.0281	0.0277		
MGN	0.0269	0.0237	0.0247	0.0226		

Table 8: Effect of noise on the RMSE of SuperMeshNet (with inductive biases), denoted as N+M, and SuperMeshNet-O (without inductive biases), denoted as O. Noise is added to node embeddings  $x_i$  and aggregated messages  $agg_i$  in MGN, trained with  $N_h=20$  and N=200 for Dataset 1.

	O	N+M
without noise	0.0269	0.0236
noise in mean	0.0312	0.0236
noise in deviation	0.0290	0.0359

strong reliance on global mean information, which is undesirable for super-resolution tasks. In contrast, SuperMeshNet (with inductive biases), denoted as N+M in Table 8, demonstrates robustness

<sup>&</sup>lt;sup>2</sup>Note that, in MPNNs such as GCN and GAT, the message-level centering cannot be employed independently since the message aggregation in Eq. (10) and the node embedding updates in Eq. (11) are integrated into a single step.

433

434

435

436 437

438

439

440

441

442

443

444

445

446

447

448

449

450

451

452

453

455

456 457

458 459 460

461

462

463

464

465

466

467

468

469

470

471

472

473

474 475

476 477

478

479

480

481

482 483 484

485

to mean perturbations but exhibits increased sensitivity to deviations. This suggests that the model with inductive biases prioritizes local deviation-related information. These findings justifies our claim that the proposed inductive biases effectively guide the model's attention to local deviations from the global mean, which are more pertinent to high-resolution reconstruction.

#### 3.7 APPLICATION TO TIME-DEPENDENT PDES AND REAL-WORLD GEOMETRY

Figures 4 and 5 present the applicability of SuperMeshNet to real-world geometry and time-dependent PDE datasets, respectively, when MGN is employed as an MPNN. Figure 4 shows the error distribution on the real-world geometry dataset, where darker blue indicates higher error. Figure 4 apparently demonstrates that SuperMeshNet, trained with only 20 HR data samples, exhibits even smaller errors than the case of the fully supervised model trained with 200 HR data samples, especially around the front region of the motorbike. Additionally, Figure 5 displays the qualitative comparisons of prediction on the time-depndent PDE dataset. The prediction by SuperMeshNet, trained with only 20 HR data samples, is even closer to the ground truth than the case of the fully supervised model trained with 200 HR data samples, particularly around the blue wake region behind the cylinder. We refer to Table 21 in Appendix P for the quantitative analysis.

#### 4 Conclusions and Limitations

In this paper, we explored the open problem of superresolution for mesh-based simulations by presenting SuperMeshNet, which judiciously harnesses complementary learning and inductive biases to achieve remarkable HR data efficiency. The complementary learning enabled effective utilization of unpaired LR data, while the inductive biases further enhanced performance across a variety of MPNN architectures. We expect that this improvement can facilitate the broader adoption of simulations across various engineering disciplines, potentially accelerating innovation by lowering the barriers to conducting complex simulations. However, while our complementary

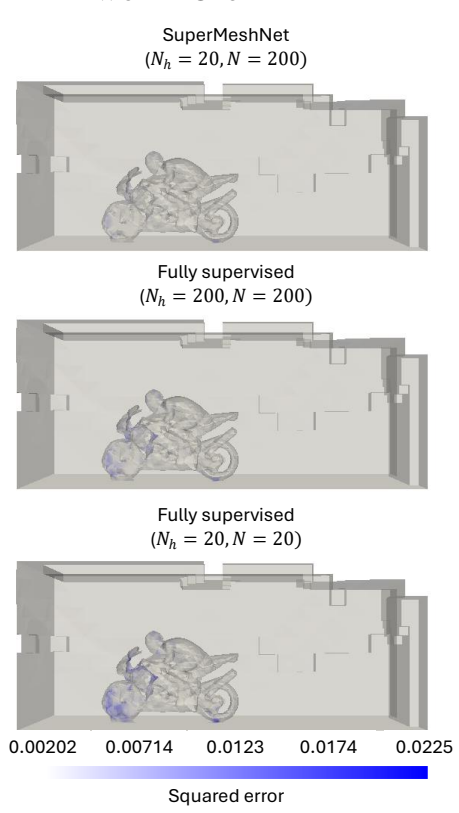


Figure 4: Comparison of squared error fields between SuperMeshNet and fully supervised baselines on real-world geometry dataset. Here,  $N_h$  and N represent the number of HR and LR training data samples, respectively. For all cases, MGN is utilized as the underlying MPNN.

learning mechanism achieves shorter training time compared to benchmark semi-supervised learning methods, it still remains slower than the case of full supervision. Further reducing the computational cost of complementary learning is a potential avenue of our future research.

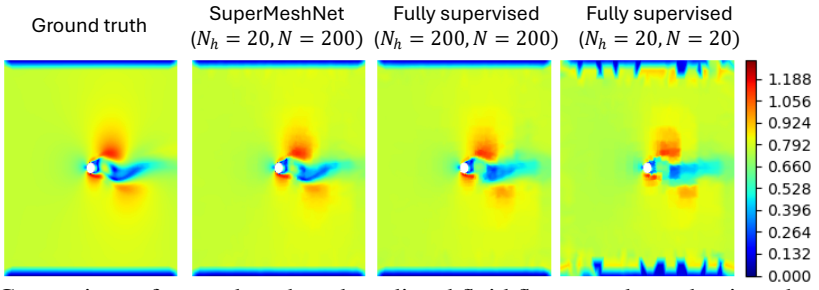


Figure 5: Comparison of ground-truth and predicted fluid flow speeds on the time-dependent PDE dataset. Here,  $N_h$  and N represent the number of HR and LR training data samples, respectively. For all cases, MGN is utilized as the underlying MPNN.

# REFERENCES

- Martin S. Alnaes, Anders Logg, Kristian B. Ølgaard, Marie E. Rognes, and Garth N. Wells. Unified form language: A domain-specific language for weak formulations of partial differential equations. *ACM Transactions on Mathematical Software*, 40, 2014. doi: 10.1145/2566630.
- Rajat Arora. Physrnet: Physics informed super-resolution network for application in computational solid mechanics. In 2022 IEEE/ACM International Workshop on Artificial Intelligence and Machine Learning for Scientific Applications (AI4S), pages 13–18, 2022. doi: 10.1109/AI4S56813.2022. 00008.
- Jimmy Lei Ba, Jamie Ryan Kiros, and Geoffrey E Hinton. Layer normalization. *arXiv preprint* arXiv:1607.06450, 2016.
- Igor A. Baratta, Joseph P. Dean, Jørgen S. Dokken, Michal Habera, Jack S. Hale, Chris N. Richardson, Marie E. Rognes, Matthew W. Scroggs, Nathan Sime, and Garth N. Wells. DOLFINx: the next generation FEniCS problem solving environment. preprint, 2023.
- Shivam Barwey, Pinaki Pal, Saumil Patel, Riccardo Balin, Bethany Lusch, Venkatram Vishwanath, Romit Maulik, and Ramesh Balakrishnan. Mesh-based super-resolution of fluid flows with multiscale graph neural networks, 2024. URL https://arxiv.org/abs/2409.07769.
- Oussama Boussif, Yoshua Bengio, Loubna Benabbou, and Dan Assouline. MAgnet: Mesh agnostic neural PDE solver. In Alice H. Oh, Alekh Agarwal, Danielle Belgrave, and Kyunghyun Cho, editors, *Advances in Neural Information Processing Systems*, 2022. URL https://openreview.net/forum?id=bx2roi8hca8.
- Ulf Brefeld, Thomas Gärtner, Tobias Scheffer, and Stefan Wrobel. Efficient co-regularised least squares regression. *Proceedings of the 23rd international conference on Machine learning*, 2006. URL https://api.semanticscholar.org/CorpusID:2025415.
- Yadi Cao, Menglei Chai, Minchen Li, and Chenfanfu Jiang. Efficient learning of mesh-based physical simulation with bi-stride multi-scale graph neural network. In Andreas Krause, Emma Brunskill, Kyunghyun Cho, Barbara Engelhardt, Sivan Sabato, and Jonathan Scarlett, editors, *Proceedings of the 40th International Conference on Machine Learning*, volume 202 of *Proceedings of Machine Learning Research*, pages 3541–3558. PMLR, 23–29 Jul 2023. URL https://proceedings.mlr.press/v202/cao23a.html.
- Weihang Dai, Xiaomeng Li, and Kwang-Ting Cheng. Semi-supervised deep regression with uncertainty consistency and variational model ensembling via bayesian neural networks. *Proceedings of the AAAI Conference on Artificial Intelligence*, 37(6):7304–7313, 2023.
- Filipe de Avila Belbute-Peres, Thomas D. Economon, and J. Zico Kolter. Combining differentiable pde solvers and graph neural networks for fluid flow prediction. In *International Conference on Machine Learning*, 2020. URL https://api.semanticscholar.org/CorpusID: 220424832.
- Huayu Deng, Xiangming Zhu, Yunbo Wang, and Xiaokang Yang. Discovering message passing hierarchies for mesh-based physics simulation, 2024. URL https://arxiv.org/abs/2410.03779.
- Meire Fortunato, Tobias Pfaff, Peter Wirnsberger, Alexander Pritzel, and Peter W. Battaglia. Multiscale meshgraphnets. *ArXiv*, abs/2210.00612, 2022. URL https://api.semanticscholar.org/CorpusID:251011532.
- Justin Gilmer, Samuel S Schoenholz, Patrick F Riley, Oriol Vinyals, and George E Dahl. Message passing neural networks. *Machine learning meets quantum physics*, pages 199–214, 2020.
- Rini Jasmine Gladstone, Helia Rahmani, Vishvas Samuel Suryakumar, Hadi Meidani, Marta D'Elia, and Ahmad Zareei. Mesh-based gnn surrogates for time-independent pdes. *Scientific Reports*, 14, 2024. URL https://api.semanticscholar.org/CorpusID:267579608.
- Will Hamilton, Zhitao Ying, and Jure Leskovec. Inductive representation learning on large graphs. *Advances in neural information processing systems*, 30, 2017.

- Pin-Yen Huang, Szu-Wei Fu, and Yu Tsao. Rankup: Boosting semi-supervised regression with an auxiliary ranking classifier. In *The Thirty-eighth Annual Conference on Neural Information Processing Systems*, 2024. URL https://openreview.net/forum?id=d2lPM1Aczs.
- Sergey Ioffe and Christian Szegedy. Batch normalization: accelerating deep network training by reducing internal covariate shift. In *Proceedings of the 32nd International Conference on International Conference on Machine Learning Volume 37*, ICML'15, page 448–456. JMLR.org, 2015.
- Thomas N. Kipf and Max Welling. Semi-supervised classification with graph convolutional networks. In *International Conference on Learning Representations (ICLR)*, 2017.
- Georgios Kostopoulos, Stamatis Karlos, Sotiris Kotsiantis, Omiros Ragos, Shailesh Tiwari, Munesh Trivedi, and Mohan L. Kohle. Semi-supervised regression: A recent review. *J. Intell. Fuzzy Syst.*, 35(2):1483–1500, January 2018. ISSN 1064-1246. doi: 10.3233/JIFS-169689. URL https://doi.org/10.3233/JIFS-169689.
- Matthew Li and Christopher McComb. Using physics-informed generative adversarial networks to perform super-resolution for multiphase fluid simulations. *Journal of Computing and Information Science in Engineering*, 22(4):044501, 02 2022. ISSN 1530-9827. doi: 10.1115/1.4053671. URL https://doi.org/10.1115/1.4053671.
- Octavi Obiols-Sales, Abhinav Vishnu, Nicholas P. Malaya, and Aparna Chandramowlishwaran. Surfnet: Super-resolution of turbulent flows with transfer learning using small datasets. In *Proceedings of the 30th International Conference on Parallel Architectures and Compilation Techniques*, PACT '21, page 331–344. IEEE Press, 2024. ISBN 9781665442787. doi: 10. 1109/PACT52795.2021.00031. URL https://doi.org/10.1109/PACT52795.2021.00031.
- OpenCFD. Openfoam v2412. 2024. URL https://openfoam.com.
- Tobias Pfaff, Meire Fortunato, Alvaro Sanchez-Gonzalez, and Peter Battaglia. Learning mesh-based simulation with graph networks. In *International Conference on Learning Representations*, 2021. URL https://openreview.net/forum?id=roNqYLO\_XP.
- Charles R. Qi, Li Yi, Hao Su, and Leonidas J. Guibas. Pointnet++: deep hierarchical feature learning on point sets in a metric space. In *Proceedings of the 31st International Conference on Neural Information Processing Systems*, NIPS'17, page 5105–5114, Red Hook, NY, USA, 2017. Curran Associates Inc. ISBN 9781510860964.
- Bruno Alves Ribeiro, João Alves Ribeiro, Faez Ahmed, Hugo Penedones, Jorge Belinha, Luís Sarmento, Miguel Anibal Bessa, and Sérgio Tavares. Simustruct: Simulated structural plate with holes dataset with machine learning applications. In *Workshop on "Machine Learning for Materials" ICLR 2023*, 2023. URL https://openreview.net/forum?id=s3tOuyR1vM7.
- Matthew W. Scroggs, Igor A. Baratta, Chris N. Richardson, and Garth N. Wells. Basix: a runtime finite element basis evaluation library. *Journal of Open Source Software*, 7(73):3982, 2022a. doi: 10.21105/joss.03982.
- Matthew W. Scroggs, Jørgen S. Dokken, Chris N. Richardson, and Garth N. Wells. Construction of arbitrary order finite element degree-of-freedom maps on polygonal and polyhedral cell meshes. *ACM Transactions on Mathematical Software*, 48(2):18:1–18:23, 2022b. doi: 10.1145/3524456.
- Yunsheng Shi, Zhengjie Huang, shikun feng, Hui Zhong, Wenjin Wang, and Yu Sun. Masked label prediction: Unified message passing model for semi-supervised classification, 2021. URL https://openreview.net/forum?id=B9t708KMr9d.
- Antti Tarvainen and Harri Valpola. Mean teachers are better role models: Weight-averaged consistency targets improve semi-supervised deep learning results. In *Proceedings of the 31st International Conference on Neural Information Processing Systems*, NIPS'17, page 1195–1204, Red Hook, NY, USA, 2017. Curran Associates Inc. ISBN 9781510860964.

Petar Veličković, Guillem Cucurull, Arantxa Casanova, Adriana Romero, Pietro Liò, and Yoshua Bengio. Graph attention networks. In *International Conference on Learning Representations*, 2018. URL https://openreview.net/forum?id=rJXMpikCZ.

- Sebastian J Wetzel, Roger G Melko, and Isaac Tamblyn. Twin neural network regression is a semi-supervised regression algorithm. *Machine Learning: Science and Technology*, 3(4): 045007, oct 2022. doi: 10.1088/2632-2153/ac9885. URL https://dx.doi.org/10.1088/2632-2153/ac9885.
- Keyulu Xu, Weihua Hu, Jure Leskovec, and Stefanie Jegelka. How powerful are graph neural networks? In *International Conference on Learning Representations*, 2019. URL https://openreview.net/forum?id=ryGs6iA5Km.
- Kazuo Yonekura, Kento Maruoka, Kyoku Tyou, and Katsuyuki Suzuki. Super-resolving 2d stress tensor field conserving equilibrium constraints using physics-informed u-net. *Finite Elements in Analysis and Design*, 213:103852, 2023. ISSN 0168-874X. doi: https://doi.org/10.1016/j.finel.2022.103852. URL https://www.sciencedirect.com/science/article/pii/S0168874X22001251.
- Zhi-Hua Zhou and Ming Li. Semi-supervised regression with co-training. In *Proceedings of the 19th International Joint Conference on Artificial Intelligence*, IJCAI'05, page 908–913, San Francisco, CA, USA, 2005. Morgan Kaufmann Publishers Inc.

# TABLE OF CONTENTS

Appendix	Main Manuscript
B. Notations	2. Methodology
C. Related Work	1. Introduction
D. Pseudo-code for Complementary Learning	2.2 Complementary Learning
E. kNN Interpolation	2.2 Complementary Learning
F. Model Architectures	2.2 Complementary Learning
G. Incorporation of Inductive Biases into MPNN Architec-	2.3 Inductive Biases for MPNNs
tures.	
H. Datasets for Experimental Evaluation	3.1 Datasets
I. Comparison of MAgNet, Fully Supervised Baseline, and	1. Introduction
SuperMeshNet	
J. Impact of Mean of Input LR Data Samples in Super-	2.3 Inductive Biases for MPNNs
resolution	
K. Comparison with Full Supervision	3.3 Comparison with Full Supervision
L. Comparison with Super-Resolution Competitors	3.4 Comparison with Super-Resolution
	Competitors
M. Comparison with Benchmark Semi-supervised Regres-	3.5 Comparison with Benchmark Semi-
sion Methods	supervised Regression Methods
O. Ablation Studies on Inductive Biases	3.6 Ablation Studies on Inductive Biases
P. Application to Time-Dependent PDEs and Real-World	3.7 Application to Time-Dependent
Geometry	PDEs and Real-World Geometry
Q. Comparison with Standard Normalization	-
R. Time Complexity	-
S. Scalability	-
T. Use of Large Language Models	-

This table provides a mapping between the appendix and the corresponding sections in the main manuscript.

# **B** NOTATIONS

Table 9: Summary of notations

Table 9: Summary of notations					
Notation	Description				
$\mu$	PDE parameters				
$F_{\theta}, G_{\phi}$	neural network models				
$u_l, u_l^q, u_l^r, u_l^s, u_l^\alpha, u_l^\beta, u_l^\gamma$	LR data samples				
$u_1$ $u_2^q$ $u_1^r$ $u_2^s$ $u_2^\alpha$ $u_2^\beta$ $u_1^\gamma$	HR data samples				
$\hat{u}_{h}, \hat{u}_{h}^{\alpha}, \hat{u}_{h}^{\beta}, \hat{u}_{h}^{\beta}, \hat{u}_{h}^{\gamma}$ $\hat{u}_{h}, \hat{u}_{h}^{\alpha}, \hat{u}_{h}^{\beta}, \hat{u}_{h}^{\gamma}$ $\hat{u}_{h}^{\beta}, \hat{u}_{h}^{\beta\gamma}, \hat{u}_{h}^{\gamma\gamma}, \hat{u}_{h}^{\gamma\alpha}$ $M_{l}$	prediction by $F_{\theta}$				
$\hat{u}_{b}^{\alpha\beta}, \hat{u}_{b}^{\beta\gamma}, \hat{u}_{b}^{\gamma\alpha}$	prediction by $G_{\phi}$				
$M_l$	LR mesh				
$M_h$	HR mesh				
$P_l$	nodal positions of LR mesh				
$P_h$	nodal positions of HR mesh				
$E_l$	edges of LR mesh				
$E_h$	edges of HR mesh				
$n_l$	number of nodes in LR mesh				
$n_h$	number of nodes in HR mesh				
n	number of nodes in graph				
$\mathcal{D}_a$	paired LR-HR training dataset				
$\mathcal{D}_b$	unpaired LR training dataset				
N	total number of training data samples				
1 <b>V</b>	= number of LR training data samples				
$N_h$	number of paired LR-HR training data sampels				
	= number of HR training data				
$\mathcal{L}_F$	loss function for training $F_{\theta}$				
$\mathcal{L}_G$	loss function for training $G_{\phi}$				
$\ell$	mean squared error				
kNN	k-nearest neighbor interpolation				
$g_l$	input graph				
${g_l\atop {}^0X_l^q}$	node feature				
${}^{0}x_{l}^{q}, {}^{H_{l}}x_{l}^{q}, {}^{0}x_{h}^{q}, {}^{H_{h}}x_{h}^{q}$	node embeddings				
$x_i$	node embedding of node $i$				
$x_j$	node embedding of node $j$				
$e_{ij}^{j}$	edge embedding between nodes $i$ and $j$				
$msg_{ij}$	message between nodes $i$ and $j$				
$agg_i$	aggregated message of node i				
$f_m$	message function				
$f_x$	node embedding update function				
$\mathcal{N}(i)$	set of neighboring nodes of $i$				
* *					

Table 9 summarizes the notations used throughout the paper.

# C RELATED WORK

756

758

759

760

761

762

764

765

766

767

768

769

770

771

772

773

774

775

776

777

778

779

781

782

783 784

785

786

787

788

789

790

791

792

793

794

795

796

797

798

799

800

801

802

803

804

805

806

808

**MPNNs for mesh-based simulations.** Conventional methods for solving PDEs, such as the FEM, typically rely on mesh-based approaches. Nevertheless, CNNs, which are not well-suited for irregular mesh-based data, have gained popularity as surrogate models, due to their simplicity and efficiency (Pfaff et al., 2021). Among notable advancements, MeshGraphNet (MGN) (Pfaff et al., 2021) represents a significant breakthrough, demonstrating that MPNNs can outperform CNN-based models for mesh-based simulation tasks. However, MGN, like other MPNNs, is constrained by a limited interaction range. Since MPNNs exchange information with immediate neighbors, extending interactions to nodes farther away requires stacking additional message passing layers. Most MPNNs suffer from over-smoothing, a phenomenon where output node embeddings become overly uniform as the number of stacked message passing layers increases, leading to performance degradation. While MGN has been reported to exhibit robustness against over-smoothing, an increased number of message passing layers still results in significantly higher computational costs. To address this limitation, researchers (Cao et al., 2023; Fortunato et al., 2022; Gladstone et al., 2024) proposed incorporating additional coarse meshes alongside the original fine mesh. This approach enables messages to propagate more efficiently across the coarse meshes while allowing the fine mesh to finely adjust node embeddings. Moreover, an attention mechanism was integrated into MGN to further refine the aggregation function, enhancing the neural network's ability to adaptively prioritize relevant information during message passing (Deng et al., 2024).

**Super-resolution for simulations.** Similarly as in surrogate models for simulations, early super-resolution models for simulations predominantly employed CNN-based image super-resolution architectures, such as SRGAN (Li and McComb, 2022) and UNet (Yonekura et al., 2023). As pioneering work, CFD-GCN (de Avila Belbute-Peres et al., 2020) introduced GCNs for the super-resolution of computational fluid dynamics (CFD) simulations. This method demonstrated both improved generalization to unseen data and enhanced cost efficiency. More recently, advanced MPNN architectures like SRGNN was applied to the super-resolution of fluid flows (Barwey et al., 2024). Despite these advancements, inductive biases tailored for MPNNs in the context of super-resolution for mesh-based simulations are largely underexplored.

Semi-supervised regression. Semi-supervised regression involves predicting real-valued output using both labeled and unlabeled datasets. Compared to semi-supervised classification, semi-supervised regression remains largely underexplored (Kostopoulos et al., 2018). A co-training approach typically splits input features into groups, with each group used to train a separate model (Brefeld et al., 2006). However, in scenarios with limited features, such as FEM-relevant data including only nodal positions and nodal values, splitting features can lead to insufficient information for accurate predictions. As an alternative, CoREG (Zhou and Li, 2005) was presented to eliminate the need for feature splitting by using two k-nearest neighbor (kNN) regressors with different distance metrics. Unfortunately, this approach is restricted to kNN regressors and is unsuitable for predicting values at the node-level. A recent method, Rankup (Huang et al., 2024), reformulated regression tasks into classification tasks to leverage a rich set of methodologies developed for semi-supervised classification. However, this technique lacks generalizability for regression tasks involving mesh-based graph data. The Mean-Teacher framework (Tarvainen and Valpola, 2017), though not originally designed for mesh-based data, has potential for dealing with mesh-based graph data. It involves teacher and student models with teacher's weights updated as the exponential moving average of the student's weights. In contrast, the recently proposed UCVME framework (Dai et al., 2023) has demonstrated superior performance over the Mean-Teacher (Tarvainen and Valpola, 2017) by incorporating uncertainty consistency and utilizing a variational model ensemble. However, because Mean-Teacher (Tarvainen and Valpola, 2017) and UCVME (Dai et al., 2023) both employ identically structured models predicting the same target, they exhibit reduced psuedo-label diversity during training. This uniformity diminishes synergy between the models and consequently hinders learning efficiency. Additionally, Twin Neural Network Regression (TNNR) (Wetzel et al., 2022) is applicable to mesh-based predictions when an appropriate model architecture is involved. However, it involves only a single twin neural network, thus lacking the synergistic benefits of mutual supervision.

# PSEUDO-CODE FOR COMPLEMENTARY LEARNING

Algorithm 1 Complementary learning **Input**: paired LR-HR dataset:  $\mathcal{D}_a = \{(I^q, u_h^q) \mid q = 1, 2, \cdots, N_h\}$ , unpaired LR dataset:  $\mathcal{D}_b = \{I^q \mid q = N_{h+1}, N_{h+2}, \cdots, N\}$ , neural network models: feature extractor  $E_c, F_\theta$ 's decoder  $D_F$ , and  $G_{\phi}$ 's decoder  $D_G$ , maximum epoch: ep, learning rate:  $\eta$ , early stopping criterion **Output:** Trained neural network models:  $E_c$ ,  $D_F$ , and  $D_G$ **for**  $epoch \leftarrow 1$  to ep **do** for  $step \leftarrow 1$  to N do Sample paired LR–HR data  $(u_l^{\alpha}, u_h^{\alpha}), (u_l^{\beta}, u_h^{\beta}) \in \mathcal{D}_a$ Sample unpaired LR data  $u_l^{\gamma} \in \mathcal{D}_b$ Compute node embeddings by  $E_c$ :  $x_{\alpha} \leftarrow E_c(u_l^{\alpha}), \ x_{\beta} \leftarrow E_c(u_l^{\beta}), \ x_{\gamma} \leftarrow E_c(u_l^{\gamma})$ Compute prediction by  $D_F$ :  $\hat{u}_h^{\alpha} \leftarrow D_F(x^{\alpha}), \ \hat{u}_h^{\beta} \leftarrow D_F(x^{\beta}), \ \hat{u}_h^{\gamma} \leftarrow D_F(x^{\gamma})$ Compute prediction by  $D_G$ :  $\hat{u}_h^{\alpha\beta} \leftarrow D_G(x^{\alpha}, x^{\beta}), \ \hat{u}_h^{\beta\gamma} \leftarrow D_G(x^{\beta}, x^{\gamma}), \ \hat{u}_h^{\gamma\alpha} \leftarrow D_G(x^{\gamma}, x^{\alpha})$ Compute loss for  $F_{\theta}$ :  $\mathcal{L}_F = \ell(\hat{u}_h^{\alpha}, u_h^{\alpha}) + \ell(\hat{u}_h^{\beta}, u_h^{\beta}) + \ell(\hat{u}_h^{\gamma}, \hat{u}_h^{\gamma\alpha} + kNN(u_h^{\alpha}; P_h^{\alpha} \to P_h^{\gamma}))$  $+\ell(\hat{u}_h^{\gamma}, kNN(u_h^{\beta} - \hat{u}_h^{\beta\gamma}; P_h^{\beta} \rightarrow P_h^{\gamma}))$ Compute loss for  $G_{\phi}$ :  $\mathcal{L}_G = \ell(\hat{u}_h^{\alpha\beta}, u_h^{\alpha} - kNN(u_h^{\beta}; P_h^{\beta} \to P_h^{\alpha})) + \ell(\hat{u}_h^{\gamma\alpha}, \hat{u}_h^{\gamma} - kNN(u_h^{\alpha}; P_h^{\alpha} \to P_h^{\gamma}))$  $+\ell(\hat{u}_{h}^{\beta\gamma}, u_{h}^{\beta} - kNN(\hat{u}_{h}^{\gamma}; P_{h}^{\gamma} \rightarrow P_{h}^{\beta}))$ Compute total loss:  $\mathcal{L} = \mathcal{L}_F + \mathcal{L}_G$ Compute gradients:  $\nabla_{\psi} \mathcal{L}$  where  $\psi$  is the parameters of  $E_c$ ,  $D_F$ , and  $D_G$ Update weights:  $\psi \leftarrow \psi - \eta \nabla_{\psi} \mathcal{L}$ end for if early stopping criterion is met then Break end if end for 

We present the pseudo-code of our complementary learning mechanism in SuperMeshNet.

**return**  $E_c$ ,  $D_F$ , and  $D_G$ 

# E kNN Interpolation

We provide a brief explanation of the kNN interpolation procedure, which projects values defined on nodes of a source mesh onto nodes of a target mesh.

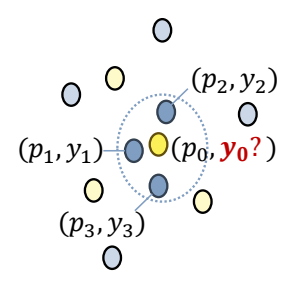


Figure 6: Schematic illustration of kNN interpolation with k=3. Yellow nodes belong to the target mesh, blue nodes to the source mesh, and the darker blue nodes indicate the k nearest neighbors of the darker yellow node. Given the positions of the k nearest source nodes  $p_i$  ( $1 \le i \le k$ ), their corresponding values  $y_i$ , and the target node position  $p_0$ , the value at the target node  $y_0$  can be estimated via weighted averaging.

- 1. **Find** *k* **nearest neighbors** (*k***NN**). For each node in the target mesh, identify the *k* closest nodes in the source mesh. For example, as illustrated in Figure 6, the darker blue nodes represent the three nearest neighbors of the darker yellow node.
- 2. **Known information.** The nodal positions of the k nearest source nodes  $p_i$   $(1 \le i \le k)$ , their values  $y_i$ , and the target node position  $p_0$ .
- 3. Unknown quantity. The value at the target node, denoted by  $y_0$ .
- 4. **Compute the target node value via weighted averaging.** The interpolation weight for each neighbor is defined as the inverse squared distance from the target node:

$$w_i = \frac{1}{d(p_0, p_i)^2}.$$

The interpolated value at the target node  $y_0$  is then obtained as

$$y_0 = \frac{\sum_{i=1}^k w_i y_i}{\sum_{i=1}^k w_i}.$$

# F MODEL ARCHITECTURES

#### F.1 MODEL ARCHITECTURES

The architecture of  $F_{\theta}$ , illustrated in Figure 7, is basically built upon SRGNN (Barwey et al., 2024), with the key difference that the MPNNs in the LR and HR processors are enriched with our proposed inductive biases. The  $G_{\phi}$ , visualized in Figure 8, extends  $F_{\theta}$  to accommodate two input samples, maintaining a comparable structure. A notable architectural feature is the use of a shared feature extractor between  $F_{\theta}$  and  $G_{\phi}$ , which helps reduce computational costs during training. A detailed description of the model architectures follows.

## F.1.1 Model architecture of $F_{\theta}$

The role of  $F_{\theta}$  is to transform LR data into HR data, which is conducted by the lowermost upsampler in Figure 7. To surpass the performance of kNN interpolation by the lowermost upsampler, we have introduced additional upsampling in latent space. Specifically, an encoder maps the physical quantities into high-dimensional latent space. The LR processor applies message passing to refine LR representations, which are then upsampled to HR latent embeddings. Subsequently, the HR processor applies additional message passing to further enhance the HR representations. Finally, a decoder maps the latent embeddings back to the physical space. The final HR output is obtained by adding the two upsampled HR fields: one from the kNN-based upsampler and the other from the latent-space upsampling pathway.

More precisely,  $F_{\theta}$  is designed to make prediction  $\hat{u}_h^q$  from an LR data sample  $u_l^q$ . The LR data sample  $u_l^q$  is input to the  $F_{\theta}$  as a form of an input graph  $g_l^q$ . More specifically, input graph  $g_l^q$ 's node feature  ${}^0X_l^q$  is the concatenation of LR data sample  $u_l^q$  and node position  $P_l^q$ . Depending on MPNN types used in the LR and HR processors (refer to Appendix G), the  $g_l^q$  may further include edge feature, which is the concatenation of positions of source and target nodes of the edge  $E_l^q$ . The  $F_{\theta}$  comprises an encoder, an LR processor, upsamplers, an HR processor, and a decoder. The encoder can be an multi-layer perceptron (MLP) that can convert low-dimensional  ${}^0X_l^q$  to high-dimensional node embeddings  ${}^0x_l^q$ . The LR processor updates the node embedding  ${}^0x_l^q$  to high-dimensional node embeddings  ${}^0x_l^q$ . The LR processor updates the node embedding  ${}^0x_l^q$  to the indicate the index of the MPNN layers enriched by our inductive biases. Here, the prescript 0 and  $H_l$  indicate the index of the MPNN layers. The node embedding  ${}^H_lx_l^q$  defined on nodes located at  $P_l^q$  is upsampled onto nodes of  $g_h^q$  positioned at  $P_h^q$  by using kNN interpolation. The HR processor similarly updates  ${}^0x_h^q$  to  ${}^H_nx_h^q$  through stacked  $H_h$  MPNN layers equipped with our inductive biases. Then, the decoder, which is an MLP, predicts low-dimensional output from  ${}^H_nx_h^q$ . Finally, the LR data sample  $u_l^q$  upsampled onto  $P_h^q$  by  $u_l^q$  by  $u_l^q$  and  $u_l^q$  upsampled onto  $u_l^q$ . The upsampled LR data sample serves as a rough estimation of the prediction, enabling the super-resolution model to focus on learning the finer details, thereby simplifying the learning task.

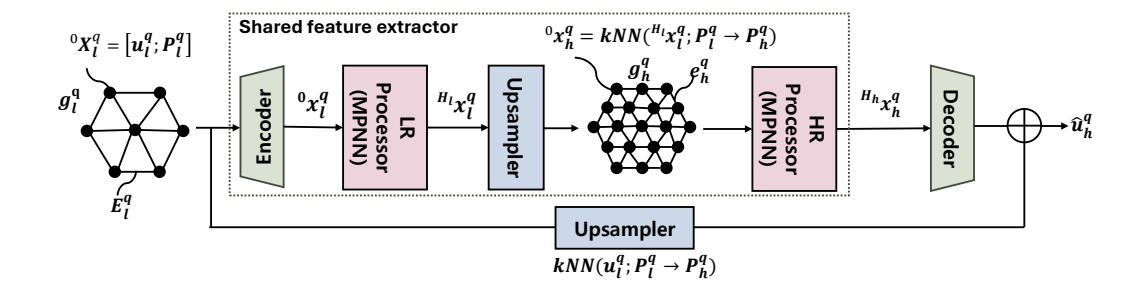


Figure 7: The schematic overview of the primary model  $F_{\theta}$ . The  $F_{\theta}$  aims to predict  $\hat{u}_h^q$  targeting HR data sample  $u_h^q$  from LR data sample  $u_l^q$ . The LR data sample  $u_l^q$  is input to the  $F_{\theta}$  as a part of node feature  ${}^0X_l^q$  of an input graph  $g_l^q$ .

## F.1.2 MODEL ARCHITECTURE OF $G_{\phi}$

 The model  $G_\phi$  is responsible for predicting the difference between two HR samples corresponding two LR inputs. Again, to go beyond simple kNN-based upsampling by upsampler in Figure 8, we have further performed latent-space processing. We have extracted latent embeddings from the two LR inputs using a shared encoder. The shared encoder is the one used for the model  $F_\theta$  depicted in Figure 7. Then, we subtracted the embeddings, and decoded the result to predict the HR difference. Here, we incorporated subtraction because the goal is to predict the difference between two HR samples. The final HR output is obtained by adding the two upsampled HR fields: one from the kNN-based upsampler and the other from the latent-space upsampling pathway. The interpolators in the Figure 8 serve only to address mesh mismatches when the two LR samples are defined on different meshes. Since the underlying computational domain geometry may vary across samples, direct point-wise operations, such as subtraction or addition, are generally infeasible. To overcome this, we apply kNN interpolation to project one mesh onto another, enabling consistent alignment between mesh structures.

More precisely, the auxiliary model  $G_\phi$  is designed to make prediction  $\hat{u}_h^{rs}$  from a pair of LR data samples  $u_l^r$  and  $u_l^s$ . More specifically, The two input LR data samples  $u_l^r$  and  $u_l^s$  are fed into the  $G_\phi$  as parts of node features of two input graphs  $g_l^r$  and  $g_l^s$ , respectively. In order to reduce computational costs,  $F_\theta$  and  $G_\phi$  share a feature extractor comprising the encoder, the LR processor, the interpolator, and the HR processor. The feature extractor returns node embeddings  $x_h^r$  and  $x_h^s$  from input graphs  $g_l^r$  and  $g_l^s$ , respectively. Then,  $x_h^s$  is subtracted from  $x_h^s$  to yield  $x_h^{rs}$ . Here, kNN interpolator is used to enable subtraction operation between two node embeddings  $x_h^r$  and  $x_h^s$  defined at different nodal positions. The  $x_h^{rs}$  is fed into the decoder, and the upsampled difference between  $u_l^r$  and  $u_l^s$  through kNN interpolation is added to the decoder's output. Here, the interpolated difference between  $u_l^r$  and  $u_l^s$  also serves as a rough estimation of the prediction  $\hat{u}_h^{rs}$ . Again, an kNN interpolator is used to enable subtraction operation between  $u_l^r$  and  $u_l^s$  defined on different nodal positions.

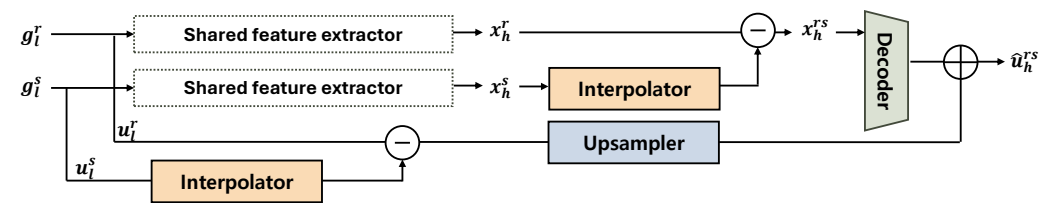


Figure 8: The schematic overview of the auxiliary model  $G_{\phi}$ . The  $G_{\phi}$  aims to predict  $\hat{u}_h^{rs}$  targeting difference between two input LR data samples  $u_l^r$  and  $u_l^s$ . The two input LR data samples  $u_l^r$  and  $u_l^s$  are fed into the  $G_{\phi}$  as parts of node features of two input graphs  $g_l^r$  and  $g_l^s$ , respectively. In order to reduce computational cost,  $F_{\theta}$  and  $G_{\phi}$  share a feature extractor in Figure 7 consisting of an encoder, an LR processor, an upsampler, and an HR processor.

# G INCORPORATION OF INDUCTIVE BIASES INTO MPNN ARCHITECTURES

This section describes how inductive biases are incorporated into each of MPNN models.

G.1 INDUCTIVE BIASES-ENRICHED GCN (KIPF AND WELLING, 2017)

$$msg_{ij} = \Theta^{T} e_{ji} x_{j}$$

$$x_{i} = agg_{i} = \sum_{j \in \mathcal{N}(i)} msg_{ij}$$

$$x_{i} \leftarrow x_{i} - \frac{1}{n} \sum_{i=1}^{n} x_{i},$$

$$(14)$$

where  $\Theta$  is a learnable parameter.

G.2 INDUCTIVE BIASES-ENRICHED GRAPHSAGE (SAGE) (HAMILTON ET AL., 2017)

$$msg_{ij} = x_{j}$$

$$agg_{i} = \frac{1}{|\mathcal{N}(i)|} \sum_{j \in \mathcal{N}(i)} msg_{ij}$$

$$agg_{i} \leftarrow agg_{i} - \frac{1}{n} \sum_{i=1}^{n} agg_{i}$$

$$x_{i} \leftarrow W_{1}x_{i} + W_{2}agg_{i}$$

$$x_{i} \leftarrow x_{i} - \frac{1}{n} \sum_{i=1}^{n} x_{i},$$

$$(15)$$

where  $W_1$  and  $W_2$  are learnable parameters.

G.3 INDUCTIVE BIASES-ENRICHED GAT (VELIČKOVIĆ ET AL., 2018)

$$\alpha_{ij} = \frac{exp(LeakyReLU(a_s^T \Theta_s x_i + a_t^T \Theta_t x_j))}{\sum_{k \in \mathcal{N}(i)} exp(LeakyReLU(a_s^T \Theta_s x_i + a_t^T \Theta_t x_k))}$$

$$msg_{ij} = \alpha_{ij}\Theta_t x_j$$

$$x_i = agg_i = \sum_{j \in \mathcal{N}(i)} msg_{ij}$$

$$x_i \leftarrow x_i - \frac{1}{n} \sum_{i=1}^n x_i,$$
(16)

where  $a_s$ ,  $s_t \Theta_s$ , and  $\Theta_t$  are learnable parameters.

G.4 INDUCTIVE BIASES-ENRICHED GRAPH TRANSFORMER (GTR) (SHI ET AL., 2021)

$$\alpha_{ij} = softmax((W_3x_i)^T(W_4x_j))$$

$$msg_{ij} = \alpha_{ij}W_2x_j$$

$$agg_i = \sum_{j \in \mathcal{N}(i)} msg_{ij}$$

$$agg_i \leftarrow agg_i - \frac{1}{n}\sum_{i=1}^n agg_i$$

$$x_i \leftarrow W_1x_i + agg_i$$

$$x_i \leftarrow x_i - \frac{1}{n}\sum_{i=1}^n x_i,$$

$$(17)$$

where  $W_1$ ,  $W_2$ ,  $W_3$  and  $W_4$  are learnable parameters.

G.5 INDUCTIVE BIASES-ENRICHED GIN (XU ET AL., 2019)

$$msg_{ij} = x_{j}$$

$$agg_{i} = \sum_{j \in \mathcal{N}(i)} msg_{ij}$$

$$agg_{i} \leftarrow agg_{i} - \frac{1}{n} \sum_{i=1}^{n} agg_{i}$$

$$x_{i} \leftarrow MLP_{\Theta}((1+\epsilon)x_{i} + agg_{i})$$

$$x_{i} \leftarrow x_{i} - \frac{1}{n} \sum_{i=1}^{n} x_{i},$$

$$(18)$$

where  $MLP_{\theta}$  is a learnable MLP and  $\epsilon$  is a learnable parameter.

G.6 INDUCTIVE BIASES-ENRICHED MESHGRAPHNET (MGN) (PFAFF ET AL., 2021)

$$e_{ij} \leftarrow MLP_e(x_i, x_j, e_{ij})$$

$$msg_{ij} = e_{ij}$$

$$agg_i = \sum_{j \in \mathcal{N}(i)} msg_{ij}$$

$$agg_i \leftarrow agg_i - \frac{1}{n} \sum_{i=1}^n agg_i$$

$$x_i \leftarrow MLP_x(x_i, agg_i)$$

$$x_i \leftarrow x_i - \frac{1}{n} \sum_{i=1}^n x_i,$$

$$(19)$$

where  $MLP_e$  and  $MLP_x$  are learnable MLPs.

# H DATASETS FOR EXPERIMENTAL EVALUATIONS

#### H.1 DATASET 1

The first dataset is inspired by simustruct (Ribeiro et al., 2023), the dataset for machine learning-based methods in structural analysis. Examples of HR and LR data samples from Dataset 1 are visualized in Figure 9. As depicted in the figure, the computational domain is a rectangle measuring  $0.25 \times 0.5$  in the x- and y-directions, containing six circular holes, each with a diameter of 0.05. For the HR mesh, the mesh size around outer four sides is  $10 \times 10^{-3}$ , while the mesh size around the circular holes is set to be  $4 \times 10^{-3}$ . For the LR mesh, the mesh size around the outer sides is  $40 \times 10^{-3}$ , and the mesh size around the circular holes is  $16 \times 10^{-3}$ .

On the computation domain, the following linear elasticity equation is solved:

$$-\nabla \cdot \sigma(u) = 0$$

$$\sigma(u) = \lambda \operatorname{tr}(\epsilon(u))I + 2\mu \epsilon(u),$$

$$\epsilon(u) = \frac{1}{2} \left( \nabla u + (\nabla u)^T \right),$$
(20)

where  $\sigma(u)$  is the stress tensor,  $\lambda$  and  $\mu$  are Lamé's elasticity parameters for the material, I is the identity tensor, tr is the trace operator on a tensor,  $\epsilon(u)$  is the symmetric strain tensor (symmetric gradient), and u is the displacement vector field.

A force of  $1\times10^8$  is applied to the top side of the rectangle in angles between  $40^\circ$  and  $140^\circ$  relative to the x-axis, while the bottom side of the rectangle is fixed to zero displacement. Lamé's first and second parameters are 1.25, and  $80.8\times10^9$ , respectively. Von Mises stress is evaluated at each node of the meshes. In order to solve the equation for each dataset, we leverage FEniCSx (Baratta et al., 2023; Scroggs et al., 2022b;a; Alnaes et al., 2014), an open-source computing platform for solving PDEs with the FEM.

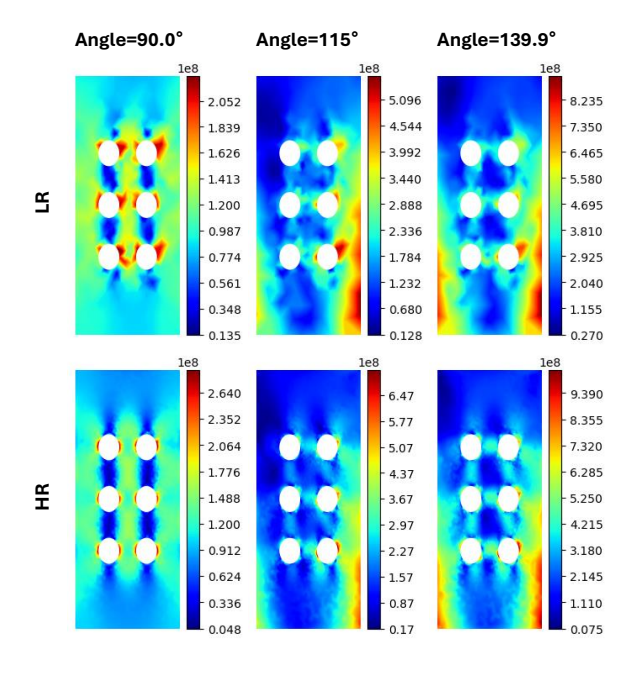


Figure 9: Examples of LR and HR data samples with various angles of applied force relative to the x-axis from Dataset 1.

#### H.2 DATASET 2

The geometry of the second dataset resembles that of the first dataset, with the primary difference being the shapes of the holes. Specifically, the holes in the second dataset are elliptical, with varying ratios between the lengths of the major and minor axes. The mesh sizes remain the same as those in Dataset 1. Similarly as in Dataset 1, the linear elasticity equation in Eq. (20) is solved. The applied force is directed along the y-axis, while all other conditions and constants remain identical to those in Dataset 1. Examples of HR and LR data samples from Dataset 2 are visualized in Figure 10.

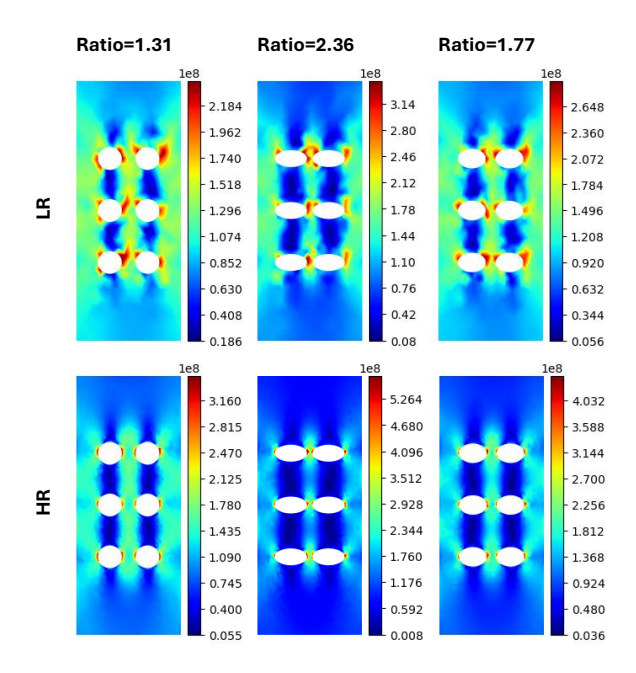


Figure 10: Examples of LR and HR data samples with various ratios between the lengths of the major and minor axes from Dataset 2.

#### H.3 DATASET 3

The geometry and mesh sizes of Dataset 3 are identical to those of Dataset 2. However, instead of solving the linear elasticity equation, the following Poisson equation is solved.

$$\nabla^2 u = 0, (21)$$

where u is an electrical potential.

The boundary conditions are defined as follows: the four outer sides are set to 0 V, while the elliptical holes have alternating boundary values. Specifically, the holes centered at (0.08, 0.15), (0.17, 0.25), and (0.08, 0.35) are assigned a value of -1 V, whereas the holes centered at (0.17, 0.15), (0.08, 0.25), and (0.17, 0.35) are assigned a value of 1 V. The magnitude of the electric field is calculated at each node of the mesh. Examples of HR and LR data samples from the Dataset 3 are visualized in Figure 11.

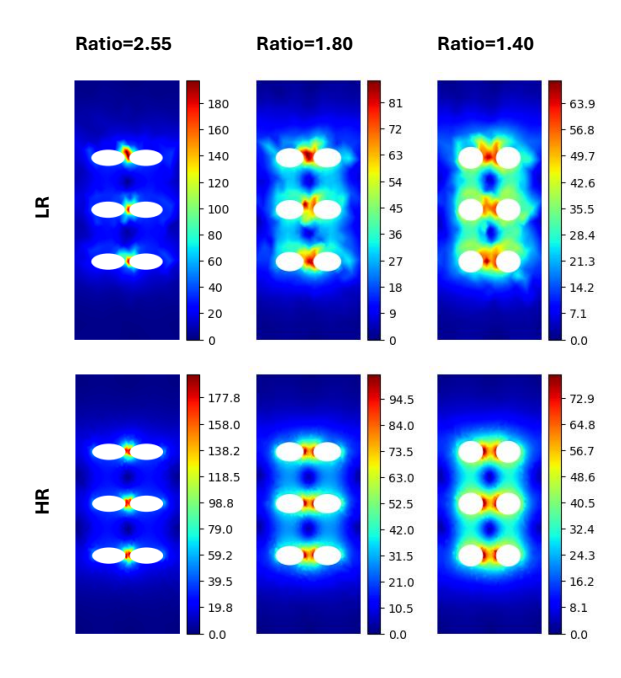


Figure 11: Examples of LR and HR data samples with various ratios between the lengths of the major and minor axes from Dataset 3.

#### H.4 TIME-DEPENDENT PDE DATASET

 Examples of HR and LR data samples from the time-dependent PDE dataset are visualized in Figure 12. As depicted in the figure, the computational domain is a square measuring  $2 \times 2$  in the x-and y-directions, containing one cylinder at the center of the domain with a diameter of 0.05. The mesh size is set to be finer around the cylinder.

On the computation domain, the following incompressible Navier-Stokes equation is solved:

$$\nabla \cdot \mathbf{v} = 0, \tag{22}$$

$$\rho \left( \frac{\partial \mathbf{u}}{\partial t} + \mathbf{u} \cdot \nabla \mathbf{u} \right) = -\nabla p + \mu \nabla^2 \mathbf{u}, \tag{23}$$

where u is velocity, p is pressure, and  $\rho$  is density,  $\mu$  is dynamic viscosity. The velocity at the left side of the square varies from 1 to 10 as time proceeds from 0 to 5. The density and the dynamic viscosity are set to be 1 and  $10^{-5}$ , respectively. A speed, a magnitude of velocity, is evaluated at each node of the meshes. In order to solve the equation, we leverage OpenFOAM(OpenCFD, 2024), an open-source CFD toolbox.

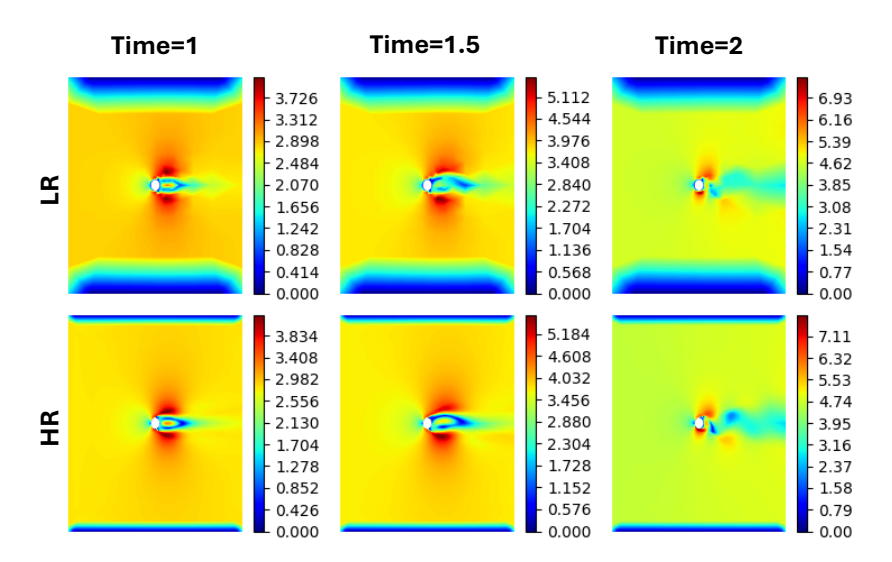


Figure 12: Examples of LR and HR data samples corresponding to multiple timestamps from the time-dependent PDE dataset.

#### H.5 REAL-WORLD GEOMETRY DATASET

An Example of HR and LR data samples from the real-world geometry dataset are visualized in Figure 13. As depicted in the figure, the computational domain is a rectangular box of size  $20 \times 8 \times 8$  in the x-, y- and z-directions, containing a rider on a motorbike. The mesh size is set to be finer around the rider and the motorbike. The dataset is built upon a bike tutorial of OpenFOAM (OpenCFD, 2024) by varying angle of attack from  $0^{\circ}$  to  $-90^{\circ}$ .

On the computation domain, the following Laplacian equation is solved:

$$\nabla^2 \phi = 0, \tag{24}$$

$$u = \nabla \phi, \tag{25}$$

where u is velocity, and  $\phi$  is velocity potential.

Then, pressure is calculated utilizing the following Bernoulli equation:

$$p = p_{ref} + \frac{1}{2}(|u_{ref}|^2 - |u|^2), \tag{26}$$

where  $p_{ref}$  and  $u_{ref}$  are the pressure and velocity at a reference location, respectively. The speed of fluid at the left side of the rectangular box is set to be 20. In order to solve the equation, we leverage OpenFOAM (OpenCFD, 2024).

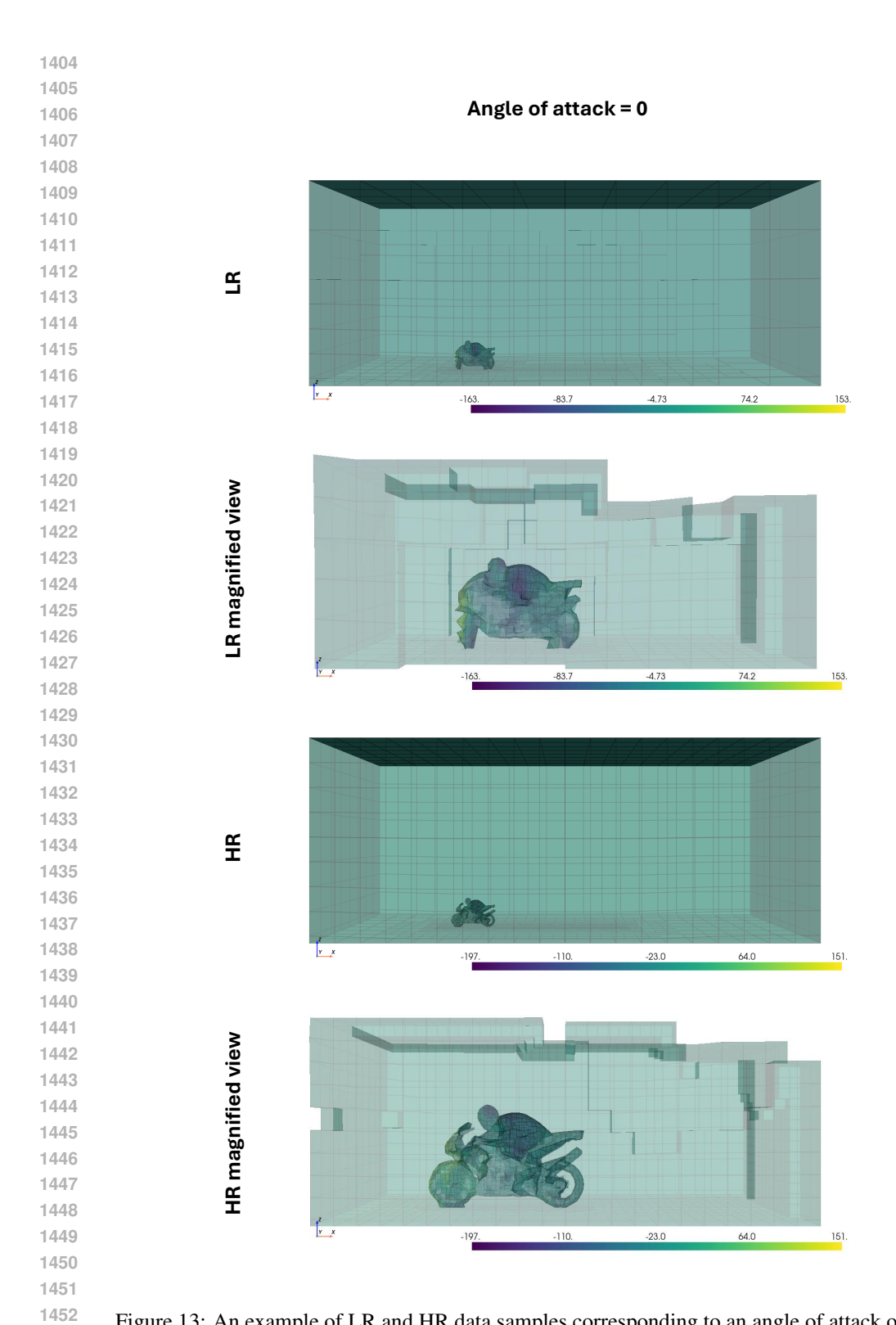


Figure 13: An example of LR and HR data samples corresponding to an angle of attack of  $0^{\circ}$  from the real-world geometry dataset.

# I COMPARISON OF MAGNET, FULLY SUPERVISED BASELINE, AND SUPERMESHNET

Table 10: RMSE comparison of MAgNet (Boussif et al., 2022), the baseline using fully supervised learning, and SuperMeshNet. SuperMeshNet is MGN with inductive biases trained with  $N_h=20$  and N=200, and the baseline is MGN without inductive biases trained with  $N_h=N=200$ . MAgNet is a zero-shot super-resolution method trained with  $N_h=0$  (i.e., no HR data) and N=200.

	Dataset 1	Dataset 2	Dataset 3
MAgNet Fully supervised learning SuperMeshNet	$0.0979 \pm 0.0009$	$0.1305 \pm 0.0007$	0.0754±0.0014
	$0.0228 \pm 0.0015$	$0.0461 \pm 0.0004$	0.0243±0.0017
	$0.0226 \pm 0.0007$	$0.0507 \pm 0.0011$	0.0245±0.0005

We empirically show the effect of HR training data over the case using zero-shot super-resolution (Boussif et al., 2022). Table 10 demonstrates that MAgNet's RMSE is far apart from that of the fully supervised baseline and SuperMeshNet across all three datasets, while being approximately up to four times higher.

# J IMPACT OF MEAN OF INPUT LR DATA SAMPLES IN SUPER-RESOLUTION

Table 11: RMSEs of MGN trained with  $N=N_h=200$ , using the following as input: LR data sample, its deviation from its mean, and the mean.

	Dataset 1	Dataset 2	Dataset 3
LR data	0.0 <b>22</b> 0 ± 0.0016	0.0.01 = 0.000.	$0.0243 \pm 0.0017$
deviation of LR data	0.0 <b>2</b> 00 ± 0.0017	$0.0463 \pm 0.0003$	$0.0241 \pm 0.0012$
mean of LR data	$0.0617 \pm 0.0012$	$0.0715 \pm 0.0014$	$0.0405 \pm 0.0006$

Our two inductive biases are motivated by the intuition that, for the super-resolution task, local deviations from the global mean are more informative than the mean itself. This intuition is empirically supported by the results in Table 11. The results demonstrate that using the deviation of the LR data samples from its mean yields an RMSE comparable to that obtained using the original LR data samples. This indicates that subtracting the mean has a negligible impact on super-resolution performance. In contrast, using only the mean of the LR data samples as input leads to a significant degradation in RMSE performance. These results suggest that the deviation from the mean plays a critical role in super-resolution, whereas the mean value alone contributes little.

# K COMPARISON WITH FULL SUPERVISION

Table 12: The RMSE of SuperMeshNet (with inductive biases) and SuperMeshNet-O (without inductive biases) trained with  $N_h=20~\mathrm{HR}$  data samples and  $N=200~\mathrm{LR}$  data samples across six MPNNs and three datasets, in comparison with two fully supervised MPNNs including 1)  $N_h=N=20~\mathrm{and}$  2)  $N_h=N=200$ . The best performer is highlighted as **bold**.

	Method			MP	'NN		
	$(N_h, N)$	GCN	SAGE	GAT	GTR	GIN	MGN
	Fully supervised	0.0874	0.0876	0.0826	0.0758	0.0819	0.0655
	(20, 20)	$\pm 0.0039$	$\pm 0.0015$	$\pm 0.0042$	$\pm 0.0068$	$\pm 0.0047$	$\pm 0.0030$
	Fully supervised	0.0575	0.0544	0.0512	0.0450	0.0381	0.0228
set	(200, 200)	$\pm 0.0035$	$\pm 0.0025$	$\pm 0.0016$	$\pm 0.0023$	$\pm 0.0027$	$\pm 0.0015$
Dataset	SuperMeshNet-O	0.0613	0.0589	0.0544	0.0451	0.0404	0.0269
Õ	(20, 200)	$\pm 0.0020$	$\pm 0.0021$	$\pm 0.0008$	$\pm 0.0020$	$\pm 0.0028$	$\pm 0.0019$
	SuperMeshNet	0.0431	0.0450	0.0457	0.0385	0.0277	0.0226
	(20, 200)	$\pm 0.0009$	$\pm 0.0010$	$\pm 0.0016$	$\pm 0.0029$	$\pm 0.0006$	$\pm 0.0007$
	Fully supervised	0.0972	0.1025	0.0983	0.0983	0.0775	0.0730
	(20, 20)	$\pm 0.0082$	$\pm 0.0052$	$\pm 0.0026$	$\pm 0.0016$	$\pm 0.0073$	$\pm 0.0075$
2	Fully supervised	0.0624	0.0633	0.0637	0.0572	0.0534	0.0461
Dataset	(200, 200)	$\pm 0.0022$	$\pm 0.0032$	$\pm 0.0013$	$\pm 0.0016$	$\pm 0.0009$	$\pm 0.0004$
ata	SuperMeshNet-O	0.0636	0.0664	0.0680	0.0631	0.0569	0.0514
Q	(20, 200)	$\pm 0.0013$	$\pm 0.0032$	$\pm 0.0023$	$\pm 0.0018$	$\pm 0.0023$	$\pm 0.0003$
	SuperMeshNet	0.0574	0.0624	0.0634	0.0600	0.0537	0.0507
	(20, 200)	$\pm 0.0003$	$\pm 0.0006$	$\pm 0.0018$	$\pm 0.0012$	$\pm 0.0015$	$\pm 0.0011$
	Fully supervised	0.0587	0.0611	0.0616	0.0513	0.0569	0.0523
	(20, 20)	$\pm 0.0038$	$\pm 0.0043$	$\pm 0.0050$	$\pm 0.0052$	$\pm 0.0016$	$\pm 0.0055$
$\alpha$	Fully supervised	0.0370	0.0340	0.0374	0.0329	0.0317	0.0243
Dataset 3	(200, 200)	$\pm 0.0029$	$\pm 0.0015$	$\pm 0.0012$	$\pm 0.0021$	$\pm 0.0022$	$\pm 0.0017$
	SuperMeshNet-O	0.0380	0.0366	0.0375	0.0363	0.0316	0.0281
Ω	(20, 200)	$\pm 0.0018$	$\pm 0.0021$	$\pm 0.0009$	$\pm 0.0023$	$\pm 0.0010$	$\pm 0.0006$
	SuperMeshNet	0.0297	0.0297	0.0310	0.0294	0.0258	0.0245
	(20, 200)	$\pm 0.0008$	$\pm 0.0014$	$\pm 0.0012$	$\pm 0.0011$	$\pm 0.0008$	$\pm 0.0005$

Table 13: The RMSE and its standard deviation of SuperMeshNet trained with  $N_h = 40$  HR data samples and N = 200 LR data samples, in comparison with a fully supervised MPNN trained with  $N_h = N = 200$ . Experiments are conducted only for cases where using  $N_h = 20$  is insufficient to outperform the fully supervised baseline.

Dataset	Method	$N_h$	N	MPNN	RMSE
2	SuperMeshNet	40	200	GTR	$0.0568 \pm 0.0015$
2	Fully supervised	200	200	GTR	$0.0572 \pm 0.0016$
2	SuperMeshNet	40	200	GIN	$0.0501 \pm 0.0004$
2	Fully supervised	200	200	GIN	$0.0534 \pm 0.0009$
2	SuperMeshNet	40	200	MGN	$0.0461 \pm 0.0011$
2	Fully supervised	200	200	MGN	$0.0461 \pm 0.0004$
3	SuperMeshNet	40	200	MGN	$0.0225 \pm 0.0003$
3	Fully supervised	200	200	MGN	$0.0243 \pm 0.0017$

In Table 12, we present the full version of Table 4 from the main manuscript, now including the standard deviation of RMSE values. In some cases, SuperMeshNet  $(N_h$ =20, N=200) yields higher RMSEs than the fully supervised baselines  $(N_h$ =N=200). In such cases, Table 13 provides additional results using SuperMeshNet with  $N_h$ =40 and N=200, where  $N_h$  is set to a slightly larger value than our default setting (i.e.,  $N_h$ =20) but still significantly smaller than 200, in comparison with the fully supervised ( $N_h$ =N=200) baselines. These results demonstrates that using only 20% of HR data samples (i.e.,  $N_h$ =40) in SuperMeshNet is sufficient to outperform the fully supervised baseline.

# L COMPARISON WITH SUPER-RESOLUTION COMPETITORS

Table 14: The RMSE and its standard deviation of MGN-based SuperMeshNet trained with varying numbers of HR data samples  $N_h$  and a fixed N=200 LR data samples in comparison with SRGNN with full supervision (N= $N_h$ =200).

Dataset	Methods	$N_h$	RMSE
1	SuperMeshNet	5 10 20 40	$\begin{array}{c} 0.0447 \pm 0.0010 \\ 0.0280 \pm 0.0013 \\ 0.0226 \pm 0.0007 \\ 0.0191 \pm 0.0021 \end{array}$
	SRGNN (Barwey et al., 2024)	200	$0.0247 \pm 0.0013$
2	SuperMeshNet	5 10 20 40	$\begin{array}{c} 0.0723 \pm 0.0018 \\ 0.0645 \pm 0.0022 \\ 0.0507 \pm 0.0011 \\ 0.0461 \pm 0.0011 \end{array}$
	SRGNN (Barwey et al., 2024)	200	$0.0487 \pm 0.0011$
3	SuperMeshNet	5 10 20 40	$\begin{array}{c} 0.0353 \pm 0.0015 \\ 0.0294 \pm 0.0010 \\ 0.0245 \pm 0.0005 \\ 0.0225 \pm 0.0003 \end{array}$
	SRGNN (Barwey et al., 2024)	200	$0.0254 \pm 0.0011$

In Table 14, we present the full version of Table 5 from the main manuscript, now including the mean and standard deviation of RMSE values for all datasets. Across all datasets, SuperMeshNet achieves a lower RMSE with a significantly smaller number of HR data samples,  $N_h$ , compared to the most recent and relevant benchmark super-resolution method, SRGNN (Barwey et al., 2024).

# M COMPARISON WITH BENCHMARK SEMI-SUPERVISED REGRESSION METHODS

Table 15: Comparison with benchmark semi-supervised regression methods in terms of the RMSE and training time (in second). Here, MGN is employed as an MPNN architecture for each method. Training is conducted when  $N_h=20$  and N=200 for each dataset. The best performer is highlighted as **bold**.

Dataset	Methods	RMSE	Training time (s)
	mean-teacher (Tarvainen and Valpola, 2017)	$0.0325 \pm 0.0016$	$694 \pm 50$
	TNNR (Wetzel et al., 2022)	$0.0624 \pm 0.0202$	$477 \pm 333$
1	UCVME (Dai et al., 2023)	$0.0293 \pm 0.0012$	$1123 \pm 102$
	SuperMeshNet-O	$0.0269 \pm 0.0019$	$503 \pm 64$
	SuperMeshNet	$0.0226 \pm 0.0007$	<b>421</b> $\pm$ 93
	mean-teacher (Tarvainen and Valpola, 2017)	$0.0499 \pm 0.0007$	$402 \pm 28$
	TNNR (Wetzel et al., 2022)	$0.0823 \pm 0.0055$	$350 \pm 90$
2	UCVME (Dai et al., 2023)	$0.0484 \pm 0.0006$	$739 \pm 59$
	SuperMeshNet-O	$0.0514 \pm 0.0003$	$306 \pm 16$
	SuperMeshNet	$0.0507 \pm 0.0011$	$250 \pm 9$
	mean-teacher (Tarvainen and Valpola, 2017)	$0.0270 \pm 0.0003$	$446 \pm 33$
	TNNR (Wetzel et al., 2022)	$0.0393 \pm 0.0027$	$437 \pm 83$
3	UCVME (Dai et al., 2023)	$0.0281 \pm 0.0013$	$700 \pm 89$
	SuperMeshNet-O	$0.0281 \pm 0.0006$	$345 \pm 10$
	SuperMeshNet	$0.0245 \pm 0.0005$	$286 \pm 18$

Table 16: Comparison with benchmark semi-supervised regression methods in terms of the RMSE and training time (in second). Here, MGN is employed as an MPNN architecture for each method. Training is conducted when  $N_h=40$  and N=200 for each dataset. The best performer is highlighted as **bold**.

Dataset	Methods	RMSE	Training time (s)
	mean-teacher (Tarvainen and Valpola, 2017) TNNR (Wetzel et al., 2022)	$0.0474 \pm 0.0007$ $0.0807 \pm 0.0074$	$427 \pm 37$ $409 \pm 143$
2	UCVME (Dai et al., 2023)	$0.0474 \pm 0.0013$	$780 \pm 89$
	SuperMeshNet-O SuperMeshNet	$0.0479 \pm 0.0005$ $0.0461 \pm 0.0011$	$348 \pm 15$ <b>292</b> $\pm 25$

Table 15 presents the full version of Table 6 from the main manuscript, now including the mean and standard deviation of RMSE and training time for all datasets under the setting of  $N_h=20~\mathrm{HR}$  data samples and  $N=200~\mathrm{LR}$  data samples. SuperMeshNet consistently results in the shortest training time across all datasets, in comparison with benchmark semi-supervised regression methods. It also achieves the lowest RMSE on Datasets 1 and 3. For Dataset 2, while SuperMeshNet yields a slightly higher RMSE, it significantly reduces training time compared to all the benchmarks. Overall, SuperMeshNet is shown to reveal strong potential in terms of both predictive accuracy and training efficiency. In Table 16, we additionally report that, for Dataset 2 with  $N_h=40~\mathrm{and}~N=200$ , SuperMeshNet still exhibits both the lowest RMSE and the shortest training time among all evaluated methods.

# N COMPARISON OF PREDICTION DIVERSITY BETWEEN UCVME AND SUPERMESHNET

Table 17: Comparison of prediction diversity between UCVME and SuperMeshNet. The prediction diversity is quantified as the root mean square of the difference between two predictions made by MGN model pairs trained by each method with  $N_h$ =20 and N=200 on each dataset. The dropout probability in UCVME is set to 0.1.

Dataset	Methods	Prediction diversity
1	UCVME (Dai et al., 2023) SuperMeshNet	$\begin{array}{c} 0.0017 \pm 0.0001 \\ 0.0200 \pm 0.0014 \end{array}$
2	UCVME (Dai et al., 2023) SuperMeshNet	$\begin{array}{c} 0.0024 \pm 0.0002 \\ 0.0514 \pm 0.0011 \end{array}$
3	UCVME (Dai et al., 2023) SuperMeshNet	$\begin{array}{c} 0.0014 \pm 0.0001 \\ 0.0294 \pm 0.0004 \end{array}$

The results in Table 17 demonstrate that SuperMeshNet exhibits consistently greater prediction diversity across all datasets, compared to the case of UCVME (Dai et al., 2023). The prediction diversity is quantified as the root mean square of the difference between two predictions made by MGN model pairs, each trained with  $N_h=20$  and N=200 on each dataset. This implies that our architectural design in complementary learning apparently more promotes diversity into the learning process than the case of UCVME.

# O ABLATION STUDIES ON INDUCTIVE BIASES

Table 18: Ablation studies on inductive biases. The RMSE of SuperMeshNet across six MPNNs under four inductive bias conditions (O: without inductive biases, N: node-level centering, M: message-level centering, and N+M: both node-level and message-level centerings) trained with  $N_h=20$  and N=200 for each dataset is compared. For each MPNN, the lowest RMSE value among the four inductive bias conditions is highlighted as **bold**.

Dataset MPNN			RM	ISE	
2 ataset	1,11	О	N	M	N + M
	GCN	$0.0613 \pm 0.0020$	$0.0431 \pm 0.0009$	-	-
	SAGE	$0.0589 \pm 0.0021$	$0.0493 \pm 0.0024$	$0.0528 \pm 0.0018$	$0.0450 \pm 0.0010$
1	GAT	$0.0544 \pm 0.0008$	$0.0457 \pm 0.0016$	-	=
1	GTR	$0.0451 \pm 0.0020$	$0.0405 \pm 0.0025$	$0.0438 \pm 0.0010$	$0.0385 \pm 0.0029$
	GIN	$0.0404 \pm 0.0028$	$0.0290 \pm 0.0026$	$0.0281 \pm 0.0015$	$0.0277 \pm 0.0006$
	MGN	$0.0269 \pm 0.0019$	$0.0237 \pm 0.0010$	$0.0247 \pm 0.0014$	$0.0226 \pm 0.0007$
	GCN	$0.0636 \pm 0.0013$	$0.0574 \pm 0.0003$	-	-
	SAGE	$0.0664 \pm 0.0032$	$0.0623 \pm 0.0005$	$0.0652 \pm 0.0009$	$0.0624 \pm 0.0006$
2	GAT	$0.0680 \pm 0.0023$	$0.0634 \pm 0.0018$	-	-
2	GTR	$0.0631 \pm 0.0018$	$0.0607 \pm 0.0009$	$0.0617 \pm 0.0025$	$0.0600 \pm 0.0012$
	GIN	$0.0569 \pm 0.0023$	$0.0523 \pm 0.0009$	$0.0549 \pm 0.0008$	$0.0537 \pm 0.0015$
	MGN	$0.0514 \pm 0.0003$	$0.0488 \pm 0.0013$	$0.0509 \pm 0.0004$	$0.0507 \pm 0.0011$
	GCN	$0.0380 \pm 0.0018$	$0.0297 \pm 0.0008$	-	-
3	SAGE	$0.0366 \pm 0.0021$	$0.0309 \pm 0.0018$	$0.0346 \pm 0.0018$	$0.0297 \pm 0.0014$
	GAT	$0.0375 \pm 0.0009$	$0.0310 \pm 0.0012$	-	-
	GTR	$0.0363 \pm 0.0023$	$0.0312 \pm 0.0008$	$0.0327 \pm 0.0006$	$0.0294 \pm 0.0011$
	GIN	$0.0316 \pm 0.0010$	$0.0261 \pm 0.0002$	$0.0268 \pm 0.0007$	$0.0258 \pm 0.0008$
	MGN	$0.0281 \pm 0.0006$	$0.0245 \pm 0.0003$	$0.0246 \pm 0.0006$	$0.0245 \pm 0.0005$

Table 19: Additional ablation studies on inductive biases. The RMSE of SuperMeshNet across six MPNNs under four inductive bias conditions (O: without inductive biases, N: node-level centering, M: message-level centering, and N+M: both node-level and message-level centerings) trained with  $N_h=80$  and N=200 for Dataset 2 is compared. For each MPNN, the lowest RMSE value among the four inductive bias conditions is highlighted as **bold**.

Dataset	MPNN	RMSE			
		О	N	M	N + M
	GCN	$0.0630 \pm 0.0017$	$0.0556 \pm 0.0006$	-	-
	SAGE	$0.0626 \pm 0.0023$	$0.0606 \pm 0.0016$	$0.0628 \pm 0.0026$	$0.0606 \pm 0.0011$
2	GAT	$0.0637 \pm 0.0005$	$0.0606 \pm 0.0016$	-	-
	GTR	$0.0606 \pm 0.0011$	$0.0560 \pm 0.0010$	$0.0574 \pm 0.0012$	$0.0554 \pm 0.0013$
	GIN	$0.0528 \pm 0.0011$	$0.0481 \pm 0.0007$	$0.0470 \pm 0.0006$	$0.0468 \pm 0.0006$
	MGN	$0.0463 \pm 0.0005$	$0.0447 \pm 0.0009$	$0.0448 \pm 0.0011$	$0.0432 \pm 0.0003$

Table 18 presents the full version of Table 7 from the main manuscript, now including the mean and standard deviation of RMSE values for all datasets. On Dataset 2, the combination of both inductive biases (N+M) occasionally results in a higher RMSE than using a single inductive bias (N). To further investigate this, Table 19 reports additional results on Dataset 2 using SuperMeshNet with  $N_h = 80$  and N = 200, where  $N_h$  is set to a slightly larger value than our default setting (i.e.,  $N_h = 20$ ) yet still significantly smaller than 200. With the larger  $N_h$ , the incorporation of both inductive biases consistently yields the lowest RMSE among the four inductive bias settings. These findings reveal the existence of a dataset-dependent threshold for  $N_h$  above which leveraging both inductive biases becomes beneficial.

Table 20: Effect of noise on the RMSE of SuperMeshNet (with inductive biases), denoted as N+M, and SuperMeshNet-O (without inductive biases), denoted as O. Noise is added to node embeddings  $x_i$  and aggregated messages  $agg_i$  in MGN, trained with  $N_h=20$  and N=200 for each dataset.

Dataset	noise condition	O	N+M
1	without noise noise in mean noise in deviation	$\begin{array}{c} 0.0263 \pm 0.0013 \\ 0.0300 \pm 0.0014 \\ 0.0285 \pm 0.0012 \end{array}$	$\begin{array}{c} 0.0214 \pm 0.0015 \\ 0.0214 \pm 0.0015 \\ 0.0328 \pm 0.0017 \end{array}$
2	without noise noise in mean noise in deviation	$\begin{array}{c} 0.0508 \pm 0.0010 \\ 0.0518 \pm 0.0012 \\ 0.0512 \pm 0.0010 \end{array}$	$\begin{array}{c} 0.0500 \pm 0.0011 \\ 0.0500 \pm 0.0011 \\ 0.0513 \pm 0.0011 \end{array}$
3	without noise noise in mean noise in deviation	$\begin{array}{c} 0.0280 \pm 0.0007 \\ 0.0292 \pm 0.0009 \\ 0.0283 \pm 0.0007 \end{array}$	$\begin{array}{c} 0.0243 \pm 0.0005 \\ 0.0243 \pm 0.0005 \\ 0.0259 \pm 0.0005 \end{array}$

Table 20 presents the full version of Table 8 from the main manuscript, now including the standard deviation of RMSE values for all datasets. Table 20 consistently presents that addition of noise to the mean component of  $x_i$  and  $agg_i$  significantly impact the RMSE of SuperMeshNet-O (without inductive biases), denoted as O in Table 20. while perturbations in the deviation component has relatively little effect. It indicates a strong reliance on global mean information, which is undesirable for super-resolution tasks. In contrast, SuperMeshNet (with inductive biases), denoted as N+M in Table 20, demonstrates robustness to mean perturbations but exhibits increased sensitivity to deviations. This suggests that the model with inductive biases prioritizes local deviation-related information. These findings justifies our claim that, regardless of datasets, the proposed inductive biases effectively guide the model's attention to local deviations from the global mean, which are more pertinent to high-resolution reconstruction.

# P APPLICATION TO TIME-DEPENDENT PDES AND REAL-WORLD GEOMETRY

Table 21: The RMSE of MGN-based SuperMeshNet trained with  $N_h=40$  HR data samples and N=200 LR data samples for the time-dependent PDE and real-world geometry datasets, in comparison with two fully supervised MGNs including 1)  $N_h=N=40$  and 2)  $N_h=N=200$ .

Dataset	Methodology	$N_h$	N	RMSE
Time-dependent PDE	SuperMeshNet fully supervised fully supervised	40 200 40	200 200 40	0.0310 0.0318 0.0599
Real-World Geometry	SuperMeshNet fully supervised fully supervised	40 200 40	200 200 40	0.0185 0.0189 0.0323

We further quantitatively evaluate the applicability of SuperMeshNet to time-dependent PDE and real-world geometry datasets. The results in Table 21 show that SuperMeshNet, trained with only 20 HR data samples, achieves even a lower error than the case of the fully supervised model trained with 200 HR data samples, demonstrating its effectiveness on to time-dependent PDE and real-world geometry datasets.

# Q COMPARISON WITH STANDARD NORMALIZATION

Table 22: Comparison of our inductive biases in SuperMeshNet with layer normalization (Ba et al., 2016) and batch normalization (Ioffe and Szegedy, 2015). All models are based on the MGN architecture and trained using complementary learning with  $N_h=20$  and N=200. The best-performing result in each case is highlighted in **bold**.

Dataset	Methods	RMSE
1	layer normalization (Ba et al., 2016) batch normalization (Ioffe and Szegedy, 2015) SuperMeshNet	$0.0310 \pm 0.0014$ $0.0165 \pm 0.0009$ $0.0226 \pm 0.0007$
2	layer normalization (Ba et al., 2016) batch normalization (Ioffe and Szegedy, 2015) SuperMeshNet	$0.0587 \pm 0.0008$ $0.0508 \pm 0.0507$ $\textbf{0.0507} \pm 0.0011$
3	layer normalization (Ba et al., 2016) batch normalization (Ioffe and Szegedy, 2015) SuperMeshNet	$0.0297 \pm 0.0013$ $0.0250 \pm 0.0003$ $0.0245 \pm 0.0005$

Similar to our inductive biases, conventional normalization techniques such as layer normalization (Ba et al., 2016) and batch normalization (Ioffe and Szegedy, 2015) also involve mean subtraction. In the context of MPNNs, layer normalization computes the mean across features within each node embedding, whereas batch normalization computes the mean across node embeddings, which is also leveraged in our inductive biases. Thus, batch normalization (Ioffe and Szegedy, 2015) is more similar to our inductive biases than layer normalization (Ba et al., 2016). Standard normalization techniques typically include additional operations such as scaling by the standard deviation and the use of learnable shift and scale parameters. The results in Table 22 demonstrate that, without these additional components, SuperMeshNet consistently outperforms layer normalization and, in some cases, even surpasses batch normalization. This suggests that centering alone—i.e., mean subtraction—acts as a crucial inductive bias for the super-resolution task.

Although our inductive bias is simpler and closely related to conventional normalization methods, it offers several key insights. First, computing the mean across nodes (as in batch normalization and SuperMeshNet) is proven to be more effective than computing the mean within each node (as in layer normalization), likely because super-resolution benefits more from local deviations from a global mean. Second, the additional components of standard normalization, such as division by standard deviation and learnable affine parameters, do not necessarily improve performance. This underscores that centering is the most essential component for super-resolution tasks.

# R TIME COMPLEXITY

 SuperMeshNet alleviates the reliance on expensive HR training data samples but incurs a longer training time compared to a fully supervised baseline. Figures 14–16 display how the training time increase and data generation time decrease—resulting from the introduction of SuperMeshNet  $(N_h=20,N=200)$ —scale with mesh size, relative to fully supervised learning  $(N_h=N=200)$ . To estimate the data generation time decrease, we measure the time required to generate 180 HR data samples by solving the PDE using a direct solver on an Intel(R) Core(TM) i7-9700K CPU @ 3.60GHz. For the training time increase, we compute the difference between the training times of MGN under fully supervised learning and SuperMeshNet, using an Intel (R) Core (TM) i9-10920X CPUs@3.50 GHz and an NVIDIA RTX A6000 GPU. The slopes in each figure are computed using the least square method. Comparison of two slopes, representing the sensitivity of training time increase and data generation time decrease to mesh size, respectively, reveals that data generation time grows more rapidly as mesh size decreases. This trend is particularly important in our target regime, where fine meshes lead to significant computational cost. We expect that for sufficiently fine meshes, the savings in data generation time will outweigh the additional training time, resulting in an overall reduction in computational costs.

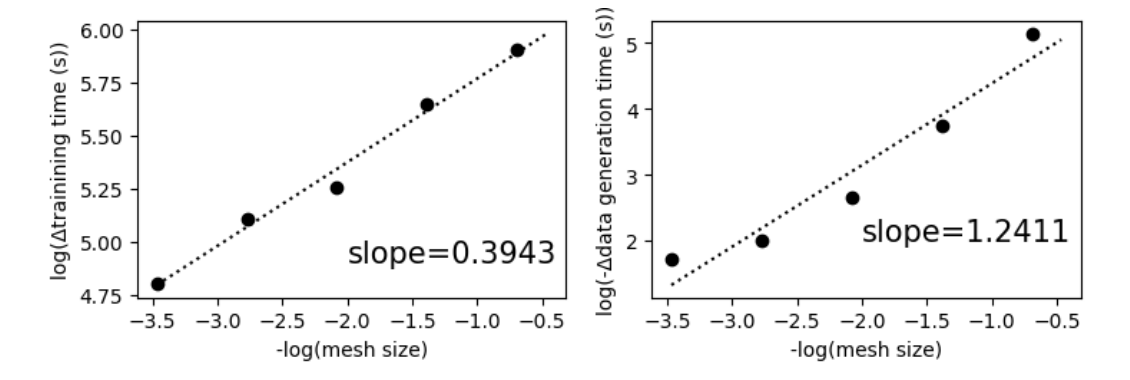


Figure 14: Training time increase (left) and data generation time decrease (right), resulting from the introduction of SuperMeshNet ( $N_h=20,\,N=200$ ), relative to fully supervised learning ( $N_h=N=200$ ) on Dataset 1 and its mesh-size variants. All experiments use MGN as the underlying MPNN architecture.

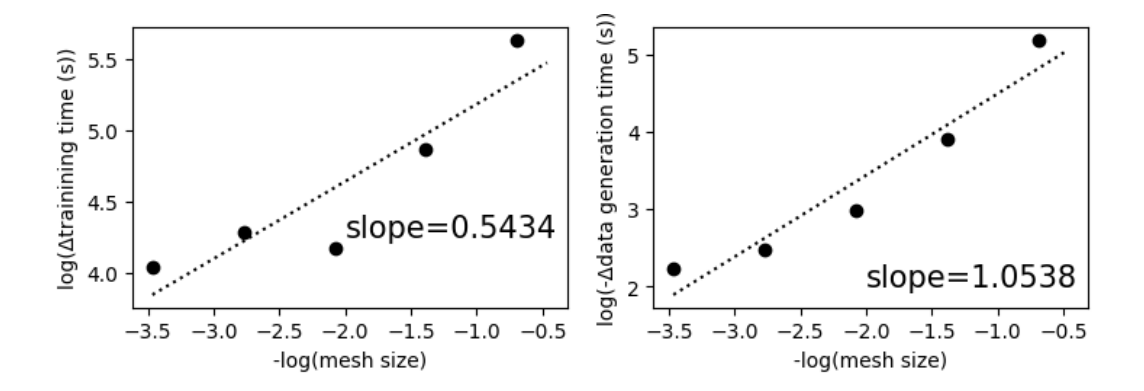


Figure 15: Training time increase (left) and data generation time decrease (right), resulting from the introduction of SuperMeshNet ( $N_h=20,\,N=200$ ), relative to fully supervised learning ( $N_h=N=200$ ) on Dataset 2 and its mesh-size variants. All experiments use MGN as the underlying MPNN architecture.

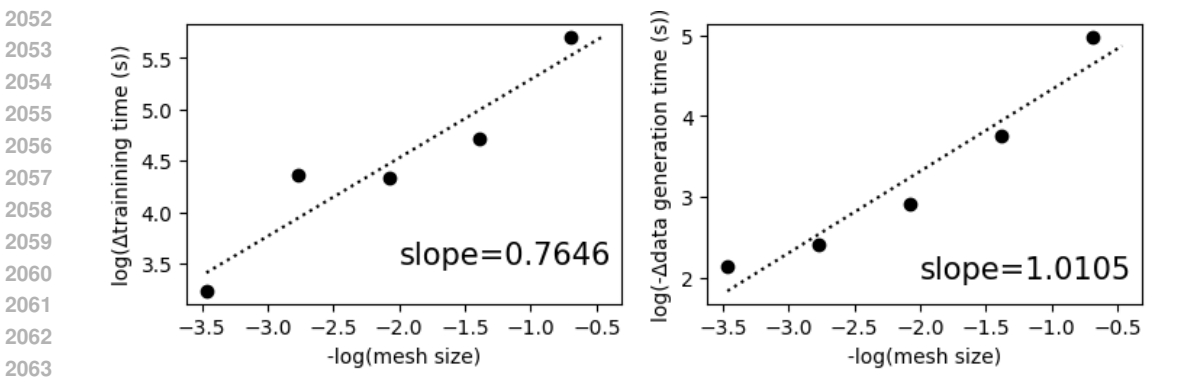


Figure 16: Training time increase (left) and data generation time decrease (right), resulting from the introduction of SuperMeshNet ( $N_h=20,\,N=200$ ), relative to fully supervised learning ( $N_h=N=200$ ) on Dataset 3 and its mesh-size variants. All experiments use MGN as the underlying MPNN architecture.

# S SCALABILITY

Table 23: Training time (in second) and RMSE of MGN-based SuperMeshNet trained with 40 HR and 200 LR data samples from Dataset 1 as a function of mesh size while fixing the magnification ratio.

Smallest mesh size	Training time (s)	RMSE
0.016	383.28	0.0112
0.008	443.34	0.0158
0.004	587.50	0.0194
0.002	710.96	0.0121

Table 24: RMSE of MGN-based SuperMeshNet trained with 40 HR and 200 LR data samples from Dataset 1 as a function of magnification ratio (HR mesh size) while fixing the LR mesh size.

	,
Magnification ratio	RMSE
$2 \times 2$	0.0099
$4 \times 4$	0.0112
$8 \times 8$	0.0689
$16 \times 16$	0.0796

In Table 23, we evaluate the scalability of our framework SuperMeshNet by measuring the training time and RMSE as a function of mesh size (while fixing the magnification ratio). These experiments have been conducted using MGN, trained with 40 HR and 200 LR data samples from Dataset 1. According to the results, the training time increases moderately as the mesh becomes finer. The RMSE tends to increase and then decrease again as the mesh becomes extremely fine. This is because we fixed the magnification ratio (the ratio between the LR mesh size and the HR mesh size) while varying both the LR mesh size and the HR mesh size. When the mesh becomes finer, the HR data samples contain more detailed features, making the LR-to-HR transformation more challenging. However, once the mesh resolution exceeds the characteristic length scale of the domain geometry, no additional details can be represented in the HR mesh. At the same time, the LR data samples already capture most of the meaningful features, and the LR-to-HR transformation becomes easier again. For comparison, we have provided Table 24, presenting experimental results where the LR mesh size is fixed while the magnification ratio (the HR mesh size) varies. In this case, the RMSE tends to monotonically increases as the HR mesh becomes finer since the LR mesh size is fixed.

# T USE OF LARGE LANGUAGE MODELS

The writing of this paper was refined with the assistance of a Large Language Model (LLM).